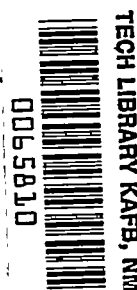


9193 6589 3616
NACA TN 2859



NATIONAL ADVISORY COMMITTEE FOR AERONAUTICS

TECHNICAL NOTE 2859

THE LANGLEY 2,000-HORSEPOWER PROPELLER DYNAMOMETER AND
TESTS AT HIGH SPEED OF AN NACA 10-(3)(08)-03
TWO-BLADE PROPELLER

By Blake W. Corson, Jr., and Julian D. Maynard

Langley Aeronautical Laboratory
Langley Field, Va.



Washington
December 1952

AFMDC
TECHNICAL LIBRARY
AFL 2011



0065810

NATIONAL ADVISORY COMMITTEE FOR AERONAUTICS

TECHNICAL NOTE 2859

THE LANGLEY 2,000-HORSEPOWER PROPELLER DYNAMOMETER AND
TESTS AT HIGH SPEED OF AN NACA 10-(3)(08)-03
TWO-BLADE PROPELLER¹

By Blake W. Corson, Jr., and Julian D. Maynard

SUMMARY

A 2,000-horsepower propeller dynamometer has been used in the Langley 16-foot high-speed tunnel to make tests of a full-scale two-blade NACA 10-(3)(08)-03 propeller for a range of blade angles from 20° to 55° at airspeeds up to 500 miles per hour. The ability of the test equipment to measure propeller characteristics accurately is confirmed by the good agreement of the results of these tests with results obtained from a theoretical analysis and from previous tests made in other wind tunnels.

The two-blade NACA 10-(3)(08)-03 propeller is very efficient at speeds where the adverse effects of compressibility are small. The maximum efficiency of 0.93, which was attained over a range of advance ratio from 1.3 to 2.0 for a constant rotational speed of 1,350 revolutions per minute, reflects the importance of designing for a minimum-induced-energy-loss loading and the use of efficient airfoil sections from the spinner surface to the propeller tip. When the helical-tip Mach number is increased from 0.90 to 1.15, the corresponding loss in propeller efficiency is about 21 percent at a blade angle of 45°.

INTRODUCTION

Tests made in the Langley 16-foot high-speed tunnel of the NACA 10-(3)(08)-03 propeller are a part of a general investigation of the aerodynamic characteristics of a series of propellers of NACA design embodying systematic variations in blade width, thickness ratio, shank form, blade section, and design lift coefficient. The primary purpose

¹Supersedes the recently declassified NACA RM L7L29, "The NACA 2000-Horsepower Propeller Dynamometer and Tests at High Speed of an NACA 10-(3)(08)-03 Two-Blade Propeller" by Blake W. Corson, Jr., and Julian D. Maynard, 1948.

of the investigation is to determine the combined influence of the propeller design parameters and air compressibility upon propeller performance at high speed. In the designing of the propellers, an attempt is made to take advantage of all available information believed to be conducive to the production of the best propeller possible within the limits of conventional aerodynamic considerations. All the propellers were designed to operate with minimum induced-energy loss when the blade angle at the 7/10 radius was 45° and the blades were operating at the design value of lift coefficient. Most of the blade designs embodied the NACA 16-series airfoil sections, which are adapted to efficient operation at high speed. Thus, both induced- and profile-drag losses are reduced to a practical minimum for the design condition.

Model propellers 4 feet in diameter were tested in the Langley 8-foot high-speed tunnel and the results showing the effects of compressibility, solidity, and camber are reported in references 1 and 2.

This paper describes the equipment used to test the full-scale propellers and its application to the determination of the aerodynamic characteristics of the NACA 10-(3)(08)-03 two-blade propeller. Since the ability to measure propeller characteristics accurately with this equipment is important for a correct evaluation of the influence of various propeller design parameters, the results of the propeller tests are compared with results obtained from a theoretical analysis and from previous tests made in other wind tunnels.

SYMBOLS

B	number of blades
b	blade width, chord
C_p	propeller power coefficient, $P/\rho n^3 D^5$
C_p'	blade-element power coefficient, dC_p/dx
C_Q	propeller torque coefficient, $Q/\rho n^2 D^5$
C_Q'	blade-element torque coefficient, dC_Q/dx
C_T	propeller thrust coefficient, $T/\rho n^2 D^4$
C_T'	blade-element thrust coefficient, dC_T/dx
c_d	blade-section drag coefficient

c_l	blade-section lift coefficient
c_{l_d}	blade-section design lift coefficient
D	propeller diameter, ft
G	Goldstein induced-velocity correction factor for finite number of blades
h	blade-section maximum thickness
J	propeller advance ratio, V/nD
J_D	propeller advance ratio based on wind-tunnel datum velocity, V_D/nD
$K = \pi^3 x G w_c \sin \phi (x - w_c \sin \phi \cos \phi)$	
L	lift, lb
l	distance measured from nose of dynamometer along shaft center line, in.
M	air-stream Mach number
M_t	helical-tip Mach number, $M \sqrt{1 + \left(\frac{\pi}{J}\right)^2}$
M_x	helical Mach number at station x , $M \sqrt{1 + \left(\frac{\pi x}{J}\right)^2}$
n	propeller rotational speed, rps
P	power absorbed by propeller, ft-lb/sec.
Q	propeller torque, ft-lb
R	resultant force, lb
r	radius at any blade section, ft
T	propeller thrust, lb
V	airspeed, ft/sec
V_D	wind-tunnel datum velocity, ft/sec

W	resultant velocity at blade section, ft/sec
W_c	coefficient of resultant velocity, $W/\pi nD$
w_c	coefficient of apparent slip velocity
w_{ic}	coefficient of induced velocity at blade section
x	fraction of propeller-tip radius
y	perpendicular distance from shaft center line to surface of dynamometer fairing, in.
α	angle of attack, deg
α_i	induced angle of attack, deg
β	blade angle at any radius, deg
$\beta_{0.75R}$	blade angle at 0.75-tip radius, deg
$\gamma = \tan^{-1} \frac{c_d}{c_l}$	deg
η	propeller efficiency, $J \frac{C_T}{C_P}$
η'	blade-element efficiency, $J \frac{C_{T'}}{C_{P'}}$
η_i'	blade-element induced efficiency
η_o'	blade-element profile efficiency
$\frac{V}{V_D}$	Glauert's velocity correction for wind-tunnel-wall interference
ρ	mass density of air, slugs/cu ft
σ	solidity, $\frac{B(b/D)}{\pi x}$
ϕ	aerodynamic helix angle, $\beta - \alpha$, deg

Subscripts:

0	first approximation for solution of w_c
1	second approximation for solution of w_c

- 2 third approximation for solution of w_c
- 3 fourth approximation for solution of w_c

APPARATUS

Langley 2,000-Horsepower Propeller Dynamometer

General arrangement.- The major components of the propeller dynamometer are two 1,000-horsepower electric motors, a heavy motor housing and column support strut, a nose housing and extension shaft, a propeller, a spinner, external fairing, thrust and torque meters, and tachometers. This description is confined to the single-rotation configuration for which the two motor shafts are coupled rigidly and drive the propeller through a single extension shaft which places the propeller disk well upstream from the flow field of the support strut.

The ultimate rating of the two motors combined is 2,280 horsepower at 2,280 revolutions per minute, but, because the value of maximum torque is fixed throughout the speed range, the maximum horsepower at any speed is numerically equal to the revolutions per minute; for example, at 960 revolutions per minute, maximum horsepower is 960.

Photographs of the dynamometer are shown as figures 1 and 2, and a diagram showing the important dimensions of the propeller dynamometer and its location with respect to the test section of the Langley 16-foot high-speed tunnel is shown in figure 3. A cutaway view of the internal mechanism is presented in figure 4.

The three subassemblies which make up the dynamometer are the fixed strut and housing, the floating thrust system, and the floating external fairing. The support strut is bolted solidly at its base to the floor of the wind tunnel and is rigidly fastened at its upper end to the heavy fixed motor housing. The sections of the support strut are the double circular-arc type approximately 17.8 percent thick with chords at the upper and lower ends of 60 and 77 inches, respectively.

The floating thrust system consists of the two motors, nose housing, extension shaft, propeller, propeller spinner, and nose spinner. The conical nose housing is fixed to the front end plate of the front motor and carries at its forward end the nose bearing (roller) which supports the shaft close behind the propeller. The motor shafts are coupled rigidly to each other, and the front-motor shaft is coupled rigidly to the extension shaft. The latter terminates at its outer end in a standard SAE number 50 spline propeller shaft. The propeller spinner is fastened to the propeller hub.

The entire floating thrust system just described is supported through four self-aligning ball bearings located on the motor shafts just outboard of each end of each motor. Each support bearing is housed in a heavy bearing block which is attached on each side through a flexure plate to the fixed motor housing. The two flexure plates which carry a bearing block are arranged to operate in tension and restrain the block rigidly against lateral motion but to allow free fore and aft rocking motion. Inasmuch as the pivot point (flexure plate) of the bearing block is about 11 inches below the center of the self-aligning support bearing, the weight carried by the bearing produces a destabilizing moment if the bearing block is rocked fore or aft. Hence, the flexure plates are designed to have such stiffness that when deflected they produce a stabilizing moment equal to the destabilizing moment produced by the weight carried. Fore and aft motion of the floating thrust system is limited by the thrust capsule to ± 0.010 inch at a point just ahead of the front motor; the neutrally stable flexure-plate support system is needed to prevent the introduction of extraneous thrust forces which otherwise would result from the fore and aft motion associated with shaft expansion.

The floating external fairing of the dynamometer is a streamlined body of revolution, coaxial with the thrust axis, which protects the nose housing and motor housing from the direct impact of the air stream. The fairing profile was calculated from a distribution of sources and sinks to produce a body of revolution with radially uniform axial velocity in the plane of the propeller. Ordinates for the fairing profile are given in table I. The entire fairing is supported from flexure rings attached to each end of the fixed motor housing. The fairing is rigidly restrained against lateral motion, but fore and aft motion is restrained by only a pneumatic drag capsule which limits motion to ± 0.010 inch and measures any axial force exerted on the floating fairing.

Control equipment.- A variable-frequency power supply is used to provide a variable-speed alternating-current drive for the dynamometer. This power supply affords an accurate speed control for the two 1,000-horsepower dynamometer motors from about 300 to 2,100 revolutions per minute with a permissible overspeed up to 2,280 revolutions per minute. A photograph of the instrument panel from which the speed of the dynamometer motors is controlled is shown as figure 5.

Thrust capsule.- As already mentioned, the free axial motion of the floating thrust system on the flexure-plate supports is restrained by only the pneumatic thrust capsule which is located inside the nose housing just ahead of the front support bearing. A cutaway view of the thrust capsule is shown in figure 6. The propeller thrust and spinner forces or any other axial forces exerted on the floating thrust system are transmitted to the propeller shaft and thence through the thrust bearings to the piston of the thrust capsule. The thrust piston is restrained laterally by flexible tie rods which allow free axial motion

but prevent rotation. Both the thrust piston and cylinder are annular in form and are concentric with the propeller shaft. The three equally spaced points of attachment by which the nose housing is fastened to the front motor are interspersed with three equally spaced cut-outs in the nose housing. Through these cut-outs, heavily constructed arms extend from the fixed motor housing to support the thrust cylinder.

Although the thrust capsule is of heavy construction, the volume of air contained in the cylinder is relatively small. The cylinder is sealed against leakage by a thin neoprene diaphragm against which the active face of the piston rests. The radial clearance between the piston and cylinder is about 0.030 inch. Thrust is measured by the air pressure within the cylinder and the active area of the piston. Thrust preload is provided by an annular cage of coil springs acting between the cylinder and piston to produce an initial thrust of about 800 pounds.

Propeller thrust may vary from a negative value up to 8,000 pounds or more and the corresponding thrust pressure will vary from about 20 pounds per square inch up to 200 pounds per square inch. With this large variation in pressure the air volume in the cylinder and consequently the axial motion of the piston would be large if the amount of air in the system were fixed. To make the thrustmeter more nearly a null instrument, a servovalve is provided to regulate the quantity of air in the thrust system.

Servovalve.- The servomechanism is a small port-type valve located at the bottom of the front face of the thrust-capsule cylinder as shown in the cutaway view in figure 6. A brief description of valves of this type is given in reference 3. When installed, the valve cylinder is integral with the fixed-thrust-capsule cylinder, and a spring forces the head of the slide back against a button on the thrust piston. Axial motion of the thrust piston is transmitted directly to the valve slide.

The valve-port arrangement is such that in the neutral position the slide cuts off one-half of the inlet port and one-half of the escape port, so that a flow of air through the valve is continuous. Air is supplied to the inlet at a closely regulated pressure of 290 pounds per square inch. Both the inlet and escape ports are 0.020 inch in diameter, and this dimension limits the axial motion of the valve slide and thrust piston to less than ± 0.010 inch throughout the range of measured thrust.

During operation an increase in thrust tends to move the thrust piston forward. This motion transmitted to the valve slide tends to open the air-supply port and close the escape port and results in an increased pressure within the valve. The increased air pressure within the valve is fed through the hollow stem of the valve slide back into the thrust cylinder where, upon acting on the neoprene diaphragm and the thrust piston, it produces a force opposing the thrust increase.

Spinner-juncture pressure.- During a test the changes in pressure inside the dynamometer fairing acting on the rear face of the propeller spinner create forces which would be included in the measurement of propeller thrust. In order to evaluate this force, two baffles are located aft of the spinner as shown in figure 7. The pressure between the two baffles is not affected by rotational speed but does vary with propeller operation and tunnel speed. This spinner-juncture pressure, the static pressure in the propeller plane well outside the slipstream, and the active baffle area determine the spinner-juncture thrust correction which has to be accounted for; this correction is hardly ever greater than 2 percent of the propeller thrust in the region of maximum efficiency.

Thrust indicators.- Two types of thrust indicators are used with the dynamometer: one visual, the other recording. Visual thrust readings are obtained with pneumatic-pressure scales (fig. 8), a highly refined pressure gage which converts pneumatic pressure from the thrust capsule into a force reading; the spinner-juncture pressure is read with a micromanometer. For a running check of the data during a test, a plot of the pneumatic-pressure-scale readings against airspeed is sufficient (constant rotational speed). For recorded thrust readings a thrust summarizer has been built and incorporated into an automatic-recording scale head. The thrust summarizer, shown in figure 9, is simply a beam with a flexure-plate fulcrum, having two sets of pressure capsules and a compensator on one side of the fulcrum and on the other side carrying a pull rod which transmits force to the scale beam.

Measurement of torque.- The torque arms which are fastened to the case of each motor extend downward through the main support strut of the dynamometer to torque capsules as shown in figure 4. Each torque arm is made up of two pipes welded together which also serve as inlet and outlet for the motor-cooling water. The torque reaction at the lower end of the torque arms is balanced by air pressure in the torque bellows shown in figure 10. The pressure in the bellows is kept proportional to the torque force by the servovalve and is transmitted to a pair of mercury manometers (fig. 11) used for visual torque readings. Preload springs are provided in each torque capsule, as shown in figure 10, so that negative torque measurements may be made. This preload is adjusted to read about 800 foot-pounds on each manometer. For recorded torque readings a device (fig. 12) was made for transferring pressures in the torque capsules into a force on the steelyard in an automatic-recording scale head.

Calibrations.- A photograph of the dynamometer stripped of the fairing and rigged for both thrust and torque calibration is presented as figure 13. Thrust calibrations are made with the propeller shaft rotating, and the calibrating thrust, therefore, must be transmitted through a thrust bearing attached to the end of the propeller shaft.

In order to reduce the amount of weight required for a calibration, a 3:1 ratio bell crank transmits to the propeller shaft a horizontal thrust three times as great as the dead-weight pan load. A typical plot of thrust-scale reading against applied load is shown in figure 14. The calibration is a straight line and the data are adjusted by the method of least squares (ref. 4). The over-all accuracy of the calibration constant is less than two parts in 1,000, and the probable error is less than 3 pounds.

A torque calibration for each of the drive motors is made in a manner similar to that for thrust. A dead-weight load is applied at the outer end of a 6-foot arm attached to the motor, and the moment produced is indicated on the torque manometer and the torque scale. A sample torque calibration of manometer reading against applied torque is shown in figure 15. The over-all accuracy of the calibration constant is better than two parts in 1,000, and the probable error is less than 2 foot-pounds for each motor.

The dynamometer is equipped with three types of tachometers, a General Electric magnetic drag tachometer for approximate visual readings with an accuracy of about ± 0.5 percent, an NACA condenser tachometer with accuracy of one part in 1,000, and a commercial Watchmaster tuning-fork tachometer with an accuracy of one part in 100,000. Nearly all tests are made at constant values of rotational speed measured with the tuning-fork tachometer, which under test conditions operates with an accuracy of about one part in 10,000. When tests must be made with varying rotational speed, the magnetic drag tachometer is used and is calibrated with the tuning-fork tachometer just prior to the test.

The wind-tunnel airspeed is calibrated by means of a standard pitot-static tube located at the propeller station. The calibration is made with the dynamometer in place but without a propeller. Calibrations are made at four different points in the propeller-disk location and the results are averaged. Accuracy of the airspeed calibration is to within three-tenths of 1 percent.

Propeller Blades

The two-blade propeller tested is designated herein by its blade design numbers, NACA 10-(3)(08)-03. The digits of the blade design numbers have the following significance: The digits in the first group of numbers represent the propeller diameter in feet; the digit in the first parentheses is 10 times the basic design lift coefficient at the 0.7 radius; the digits in the second parentheses are the thickness ratio in percent at the 0.7 radius; and the digits in the third group represent the solidity per blade at the 0.7 radius. The NACA 16-series blade sections are used, and the propeller is designed to obtain very high

aerodynamic efficiency, all but the most elementary strength considerations being disregarded. Efficient airfoil sections extend to the spinner surface for this propeller, which is designed to have the Betz minimum-induced-energy-loss loading (ref. 5) when operating at a blade angle of 45° at the 0.7 radius and at an advance ratio of 2.1. The design procedure used consists in finding the optimum loading when the profile drag is assumed to be zero and then determining the best blade shape for that loading when a thickness distribution is assumed. Blade-form curves for this design are shown in figure 16, and figure 17 is a photograph of one of the blades.

TESTS

Thrust, torque, and rotational speed were measured during tests at fixed blade angles of 20° , 25° , 30° , 35° , 40° , 45° , 50° , and 55° at the 0.75 (45-inch) radius. A constant rotational speed was used for most of the tests, and a range of advance ratio $\left(J = \frac{V}{nD}\right)$ was covered by changing the tunnel airspeed, which could be varied from about 60 to 500 miles per hour.

The range of blade angles covered at the various rotational speeds used in the tests is shown in table II. At the higher blade angles the complete range of advance ratio could not be covered at the higher rotational speeds because of power limitations. In order to obtain propeller characteristics at maximum tunnel airspeeds, a blade angle of 45° was chosen for which the peak-efficiency operating condition could be attained when the tunnel airspeed was at or near the maximum and the dynamometer was operating at its maximum power and rotational speed. For these tests, at a blade angle of 45° , the rotational speed was varied to obtain data from peak efficiency to the zero-torque operating condition.

REDUCTION OF DATA

Thrust.— The propeller data presented in this paper represent, as nearly as could be obtained, the performance in free air of only the propeller blades from the spinner surface to the blade tips. In making a test, the dynamometer complete with fairing and spinners, but without propeller blades, is operated in the wind tunnel and the tare spinner force and spinner-juncture pressure are measured. The propeller blades are then installed on the dynamometer and the propeller is operated. The propeller thrust is taken as the indicated thrust with propeller minus the spinner-tare thrust and minus the force increase created by any change in spinner-juncture pressure, all quantities being treated algebraically.

Tunnel-wall correction.- Because the relation between airspeed and propeller thrust is not the same in a wind tunnel as in free air, a correction to the tunnel airspeed must be applied to reduce the wind-tunnel propeller data to the free-air condition. This correction has been derived theoretically by Glauert in reference 6. A plot of Glauert's correction for a 10-foot-diameter propeller operating in a closed 16-foot circular wind tunnel is presented in figure 18. A velocity survey rake as shown in figure 3 was installed at the plane of the propeller between the propeller disk and the tunnel wall. Velocity measurements made with the rake were used to verify the calculated theoretical correction. A further check, which showed the theory to be valid, is reported in reference 7. As shown in figure 18, the magnitude of the correction at peak efficiency is generally less than 1 percent. Under extreme conditions of low speed and high thrust, the correction sometimes is of the order of 4 percent. All the data presented represent the characteristics of only the propeller blades operating in free air.

Torque.- No correction to the indicated torque reading was found necessary. The dynamometer torque was unaffected by tunnel operation, and tare torque due to bearing friction was found to be negligible.

Accuracy.- The propeller data presented in this paper are believed to involve a total error of less than 1 percent.

RESULTS AND DISCUSSION

Basic data.- The basic data are shown as faired curves of thrust coefficient, power coefficient, and propeller efficiency plotted against advance ratio and are presented in figures 19 to 25 for the two-blade NACA 10-(3)(08)-03 propeller. Test points are shown in the figures giving thrust and power coefficients. The variation of air-stream Mach number and helical-tip Mach number with advance ratio is shown in the figures giving propeller efficiency.

The envelope curves of propeller efficiency at the different test rotational speeds are shown in figure 26. The curves show very high efficiencies, particularly at the lower rotational speeds where the adverse effects of compressibility are small. At rotational speeds between 1,140 and 1,600 revolutions per minute, the envelope efficiencies were above 0.90 over the range of advance ratio of the tests. A maximum efficiency of 0.93 was attained over a range of advance ratio from 1.3 to 2.0 for a constant rotational speed of 1,350 revolutions per minute. At the higher rotational speeds the envelope efficiencies become less, and at 2,160 revolutions per minute the maximum efficiency reached was about 0.85 at an advance ratio of 0.85.

In figure 27 the envelope efficiency of the two-blade NACA 10-(3)(08)-03 propeller at 1,350 revolutions per minute is compared with the optimum efficiency of a two-blade propeller with the Betz minimum-induced-energy-loss loading. The curve of optimum efficiency was calculated by a method in which all profile-drag losses are neglected (ref. 8) for a two-blade propeller operating at the same values of power coefficient as were obtained with the NACA 10-(3)(08)-03 propeller. The curves in figure 27 indicate that the blade loading for the propeller tested may be considered very near the optimum and that the profile-drag losses amount to about 3 percent in the range of advance ratio for which the NACA 10-(3)(08)-03 propeller was designed. The highest efficiency (approximately 0.93) reflects the importance of designing for a minimum-induced-energy-loss loading and reflects the use of efficient airfoil sections from the spinner surface to the propeller tip.

One of the principal reasons for the high efficiency of the NACA 10-(3)(08)-03 propeller is that efficient airfoil sections extend to the spinner surface. Both theoretical analyses (refs. 5 and 8) and experiments (refs. 9, 10, and 11) have shown that the thick inner sections of conventional cylindrical-shank propellers are one of the chief sources of blade-drag loss, especially at high values of advance ratio. The results presented in reference 9 show that thick shank sections reduce the maximum efficiency of an NACA 10-(5)(08)-03 propeller by approximately 5 percent, and it is reasonable to assume that the maximum efficiency of the NACA 10-(3)(08)-03 propeller would have been reduced several percent if efficient airfoil sections had not extended to the spinner surface.

Effect of compressibility on maximum efficiency.- The variation of envelope efficiency with helical-tip Mach number is shown in figure 28 for the two-blade NACA 10-(3)(08)-03 propeller at the different rotational test speeds. The variation of air-stream Mach number with helical-tip Mach number at each rotational speed is also shown in figure 28. A curve drawn tangent to the efficiency envelopes in figure 28 would show the maximum efficiency obtainable at appropriate combinations of rotational speed and air-stream Mach number. Unfortunately, the envelopes at the higher rotational speeds could not be extended further because of the power limitations previously mentioned. At a constant air-stream Mach number of 0.38, the curves in figure 28 show that the envelope efficiencies drop about 10 percent for a change in helical-tip Mach number from about 0.87 to 1.105. From a helical-tip Mach number of 0.62 to 0.87, the envelope efficiencies change very little.

The highest tip speeds shown in figure 28 were obtained at comparatively low forward speed, and it should be pointed out that such data may not be adequate when used in estimating efficiencies for higher forward speeds because the radial variation of Mach number will not be correct. For the same helical-tip Mach number but at a higher air-stream

Mach number, the inboard sections of a propeller blade must necessarily be designed very carefully to avoid compressibility losses over these sections. A very extensive test program would be required to obtain propeller data having representative variations of Mach number along the blade for each value of forward speed and advance ratio. However, the data shown in figure 25 were obtained to indicate the losses which might be expected at high tip speeds and forward speeds as high as could be attained in the tunnel. With these data and the data in figures 19 to 22, the effect of compressibility on maximum efficiency for a blade angle of 45° may be obtained. Figure 29 shows that the maximum efficiency of the NACA 10-(3)(08)-03 propeller was slightly more than 0.92 for helical-tip Mach numbers from 0.64 to 0.90. From a helical-tip Mach number of 0.90 to 1.15, the maximum efficiency dropped 21 percent, which shows that the critical tip Mach number for the NACA 10-(3)(08)-03 propeller is about 0.90. The variation of air-stream Mach number with helical-tip Mach number is also included in figure 29, and this curve shows that for air-stream Mach number values in excess of 0.55 the maximum propeller efficiency will be less than 0.90 for the design blade angle of 45° .

Comparison with results obtained in other wind tunnels.- A model of the NACA 10-(3)(08)-03 propeller was tested in the Langley 8-foot high-speed tunnel, and the results are presented in reference 1. The data from the tests of this model propeller, which was 4 feet in diameter (NACA 4-(3)(08)-03), have been compared in figures 29 and 30 with the data from the tests of the full-scale propeller. In figure 29 a curve showing the effect of compressibility on maximum efficiency of the model propeller at a blade angle of 45° may be compared with efficiency values found for the full-scale propeller. From a helical-tip Mach number of 0.65 to 0.90, the maximum efficiency of the model propeller is 1 to 2 percent higher, and at the higher helical-tip Mach numbers the difference in maximum efficiency for the model and full-scale propellers is smaller. The critical-tip Mach number (about 0.9) is approximately the same for both the model and the full-scale propellers. Figure 30 shows a comparison of the envelope efficiencies of the full-scale and model propellers over a range of air-stream Mach numbers from 0.16 to 0.53. Over the range of advance ratio from 1.7 to 2.7 the values of envelope efficiency for the model propeller are slightly higher ($\frac{1}{2}$ to $1\frac{1}{2}$ percent) than those for the full-scale propeller. At advance ratios below 1.5, the envelope efficiency of the model propeller was less than that for the full-scale propeller, and the difference amounted to $4\frac{1}{2}$ percent at an advance ratio of 0.9. At the higher advance ratios the differences in envelope efficiency are perhaps within the limits of experimental accuracy of the two sets of data, but at the lowest advance ratio of the tests the difference is difficult to explain. However, the discrepancies may possibly be accounted for by the following factors:

(1) The Reynolds numbers for the model tests were lower than those for the full-scale tests.

(2) The spinner diameter was 0.217 of the propeller diameter in the full-scale tests and 0.333 of the propeller diameter in the model tests.

(3) The nose-blower cowling used in the model tests contributed both thrust and torque to the measured forces, and the tare corrections, especially at low advance ratios, were increased because of the effect of the blower.

The comparison with model test results may be considered very good when the differences in the model configurations and the testing techniques are taken into account.

Figure 31 shows a comparison of the envelope efficiency obtained in the Langley propeller-research tunnel (ref. 12) and in the Langley 16-foot high-speed tunnel for a three-blade NACA 10-(3)(08)-03 propeller. Because discussion of the results from tests of the three-blade propeller is beyond the scope of this paper, the individual test data are not presented. However, since the three-blade configuration was the only one tested in the Langley propeller-research tunnel, the comparison in figure 31 is presented as a check on the results obtained by using the 2,000-horsepower dynamometer in the Langley 16-foot high-speed tunnel. Over the range of advance ratio from 1.6 to 3.3 the envelope efficiency obtained in the Langley 16-foot high-speed tunnel was only 1/2 percent greater than that obtained in the Langley propeller-research tunnel. This result indicates almost perfect agreement in that the Langley 16-foot high-speed tunnel tests were made at speeds where compressibility effects were advantageous. The good agreement of the two sets of data mutually confirms the reliability of the testing techniques used at both the Langley propeller-research tunnel and the Langley 16-foot high-speed tunnel.

Calculated results from a theoretical analysis.- Values of thrust, torque, and efficiency have been calculated for three conditions of operation for the two-blade NACA 10-(3)(08)-03 propeller by using a strip-theory analysis. Airfoil data for a few values of camber c_{7d} and for several thickness ratios for the NACA 16-series airfoil sections are available for Mach numbers up to about 0.80 (see ref. 13). These data were used for this analysis by selecting conditions of propeller operation for which the helical-tip Mach numbers of the blade sections did not exceed 0.75. The equations and procedure used in the theoretical analysis are presented in the appendix.

The three conditions of propeller operation chosen for this analysis were for values of advance ratio of 1.18, 2.20, and 3.22 at a constant rotational speed of 1,140 revolutions per minute. These values of advance

ratio correspond to the maximum-efficiency condition at blade angles of 30° , 45° , and 55° , respectively. The results of this analysis are presented in figure 32, which shows the calculated radial distribution of thrust coefficient, power coefficient, efficiency, and helical Mach number for each of the three conditions of propeller operation. The thrust and power loading for maximum-efficiency operation at the 55° blade angle is much higher than that for the lower blade angles, and a larger proportion of the load is carried by the inboard sections for the high-blade-angle condition of operation. This inboard shift of the load for the high-blade-angle condition results in lower efficiencies for the inboard sections and slightly higher efficiencies for the outboard sections of the propeller blade. The thrust-loading curve for maximum-efficiency operation at the lowest blade angle of 30° shows that the tip sections as well as the sections nearest the shank carry less load than they do for maximum-efficiency operation at the design blade angle of 45° ; the sections from 0.4 to 0.8 of the tip radius carry more of the thrust load than for the design condition of operation. This shift in the thrust loading results in lower efficiencies for all sections along the blade except those nearest the shank.

The theoretical analysis makes it possible to evaluate the profile and induced losses along the propeller blade by calculating the elemental profile efficiency η_0' and the elemental induced efficiency η_1' . Figure 33 shows the distribution of these elemental efficiencies along the blade for the three chosen conditions of propeller operation. Profile losses are slightly greater over the inboard sections and induced losses are slightly greater over the outboard sections of the propeller for all three conditions of operation. For maximum-efficiency operation at a blade angle greater than the design blade angle of 45° , both the profile and induced losses become much greater over the inboard sections of the blade. For maximum-efficiency operation at a blade angle less than the design blade angle of 45° , induced effects account for the greater part of the losses along the blade except those nearest the shank and at the tip.

Comparison of experimental and calculated results.- It has been shown in reference 14 that the performance of a propeller can be accurately calculated if the airfoil section characteristics are known. Although the variation of airfoil characteristics with Mach number is not taken into account in the calculations presented in reference 14, an agreement of experimental and calculated results presented herein would serve as a check on the ability of the dynamometer to measure propeller characteristics accurately. The thrust- and power-loading curves in figures 32(a) and 32(b), respectively, were integrated from the propeller spinner to the propeller tip, and the resulting values of thrust and power coefficients together with the calculated values of efficiency are shown in table III. For comparison, the corresponding values as found in the propeller tests are also shown in table III. The

calculated and experimental values of efficiency are in very close agreement. Also, the values of thrust and power coefficient are in good agreement, except for the condition of operation at an advance ratio of 2.20 where the difference amounted to approximately 4 percent for the power coefficient and 5 percent for the thrust coefficient. The agreement between calculated and experimental values is considered good.

CONCLUSIONS

The Langley 2,000-horsepower propeller dynamometer has been used to make wind-tunnel tests of a full-scale two-blade NACA 10-(3)(08)-03 propeller for a range of blade angles from 20° to 55° at airspeeds up to 500 miles per hour. The results of these tests and comparisons with results obtained from a theoretical analysis and from previous tests made in other wind tunnels led to the following conclusions:

1. The two-blade NACA 10-(3)(08)-03 propeller is very efficient at speeds where the adverse effects of compressibility are small. The maximum efficiency of 0.93, which was attained over a range of advance ratio from 1.3 to 2.0 for a constant rotational speed of 1,350 revolutions per minute, reflects the importance of designing for a minimum-induced-energy-loss loading and the use of efficient airfoil sections from the spinner surface to the propeller tip.
2. When the helical-tip Mach number is increased from 0.90 to 1.15, the corresponding loss in propeller efficiency is about 21 percent at a blade angle of 45° .
3. The ability of the test equipment to measure propeller characteristics accurately is confirmed by:
 - (a) The good agreement of the full-scale propeller results reported herein with those obtained for a 4-foot-diameter model propeller in the Langley 8-foot high-speed tunnel, especially at high speed.
 - (b) The good agreement of results of tests made in the Langley 16-foot high-speed tunnel and in the Langley propeller-research tunnel for identical propellers.
 - (c) The good agreement between experimental results and results calculated by a strip-theory analysis.

Langley Aeronautical Laboratory,
National Advisory Committee for Aeronautics,
Langley Field, Va., February 16, 1948.

APPENDIX

EQUATIONS AND PROCEDURE USED IN MAKING THE STRIP-THEORY

ANALYSIS OF THE NACA 10-(3)(08)-03 PROPELLER

For each value of advance ratio under consideration, curves of c_l against α and of $\tan \gamma$ against c_l are plotted for each radial station along the propeller blade by a process of cross-plotting and interpolation of the airfoil characteristics. It must be remembered that each of these curves may be used only for the particular value of Mach number, camber, and thickness ratio of the radial station under consideration. After plotting these curves of c_l against α and $\tan \gamma$ against c_l , the calculation of the elemental values of thrust and power coefficients can be made.

Figure 34 shows a vector diagram of the forces acting on a blade element and also the velocity vectors which are made nondimensional. From the vortex theory of propellers with Goldstein's corrections for a finite number of blades, the coefficient of induced velocity at a blade element is shown to be

$$w_{ic} = \frac{\sigma c_l W_c}{4G \sin \phi}$$

and from the vector diagram the apparent axial velocity of the helicoid at a blade element is

$$W_c = \frac{w_{ic}}{\cos \phi} = \frac{\sigma c_l W_c}{4G \sin \phi \cos \phi} \quad (1)$$

The following expression for W_c may be obtained from the vector diagram:

$$W_c = \frac{x}{\cos \phi} - w_c \sin \phi$$

Substituting this expression for W_c into equation (1) gives

$$W_c = \frac{\frac{x \sigma c_l}{\sin \phi \cos \phi}}{4G \cos \phi + \sigma c_l} \quad (2)$$

Another equation containing w_c obtained from the vector diagram is

$$\tan \phi = \frac{\frac{J}{\pi} + w_c}{x} \quad (3)$$

A value of w_c which will satisfy equations (2) and (3) must be found for each radial station along the blade. The solution is made by successive approximations. As a first approximation the induced angle of attack α_1 is assumed to be zero, and w_c is therefore equal to zero. Then from equation (3)

$$\tan \phi_0 = \frac{\frac{J}{\pi} + 0}{x} = \frac{J}{\pi x}$$

and

$$\alpha_0 = \beta - \phi_0$$

(Subscripts 0, 1, 2, and 3 denote first, second, third, and fourth approximations, respectively, for solution of w_c .) By using ϕ_0 , Goldstein's factor may be found from a chart (ref. 8) showing G as a function of ϕ ; by using α_0 , c_{l0} may be found from the airfoil characteristic curves previously mentioned. Since the solidity σ is known, equation (2) may be solved to find a value $(w_c)_0$. Then by using $(w_c)_0$ in equation (3) a second approximation may be made

$$\tan \phi_1 = \frac{\frac{J}{\pi} + (w_c)_0}{x}$$

and

$$\alpha_1 = \beta - \phi_1$$

By using these new values (ϕ_1 and α_1) to find G_1 and c_{l1} , equation (2) is solved again to find $(w_c)_1$. Next, a plot is made of assumed values of w_c against the calculated values, and since the assumed value must be equal to the calculated value to satisfy equations (2) and (3), a third value $(w_c)_2$ may be found from the plot as shown in figure 35. By using $(w_c)_2$ in equation (3) a third approximation may be made

$$\tan \phi_2 = \frac{\frac{J}{\pi} + (w_c)_2}{x}$$

and

$$\alpha_2 = \beta - \phi_2$$

By using the new values G_2 and c_{l2} , equation (2) is solved again and $(w_c)_3$ is found. Usually this value $(w_c)_3$ is found to be equal to the assumed value $(w_c)_2$ and no further computations for w_c are necessary. However, if this is not the case, the value $(w_c)_3$ is plotted as shown in figure 35 and a curve is drawn through the three points. The intersection of this curve with the straight line (slope, 1.0) through the origin gives a value of w_c which will be found to satisfy equations (2) and (3).

After the correct value of w_c is found for each radial station along the propeller blade, the elemental thrust and power coefficients may be found by setting up the equations for dL , dR , dT , and dQ .

The lift on a blade element for B blades is

$$dL = \frac{1}{2} \rho W^2 c_l b B dr \quad (4)$$

In equation (4), W is the resultant velocity at the blade element and may be expressed as follows:

$$W = \pi n D w_c = \pi n D \left(\frac{x}{\cos \phi} - w_c \sin \phi \right)$$

Substituting this expression for W into equation (4) and simplifying results in

$$dL = \rho n^2 D^4 K dx \quad (5)$$

where

$$K = \pi^3 x G w_c \sin \phi (x - w_c \sin \phi \cos \phi)$$

Then

$$dR = \frac{dL}{\cos \gamma} = \rho n^2 D^4 \frac{K}{\cos \gamma} dx \quad (6)$$

$$dT = dR \cos (\phi + \gamma) = \rho n^2 D^4 \frac{K}{\cos \gamma} \cos (\phi + \gamma) dx \quad (7)$$

$$\frac{dQ}{r} = dR \sin (\phi + \gamma)$$

$$dQ = \rho n^2 D^4 \frac{Kr}{\cos \gamma} \sin (\phi + \gamma) dx$$

$$dQ = \rho n^2 D^5 \frac{Kx}{2} \frac{\sin (\phi + \gamma)}{\cos \gamma} dx \quad (8)$$

From equation (7) and the definition of thrust coefficient

$$C_T' = \frac{dC_T}{dx} = K \frac{\cos(\phi + \gamma)}{\cos \gamma} \quad (9)$$

From equation (8) and the definition of torque coefficient

$$C_Q' = \frac{dC_Q}{dx} = \frac{Kx}{2} \frac{\sin(\phi + \gamma)}{\cos \gamma}$$

but

$$C_P' = 2\pi C_Q'$$

and, therefore,

$$C_P' = \pi Kx \frac{\sin(\phi + \gamma)}{\cos \gamma} \quad (10)$$

The blade-element efficiency is

$$\eta' = J \frac{C_T'}{C_P'} = \frac{J}{\pi x \tan(\phi + \gamma)} \quad (11)$$

Equation (11) may be written as follows:

$$\eta' = \frac{1}{\tan(\phi + \gamma)} \frac{1}{x} \left[\left(\frac{J}{\pi} + w_c \right) - w_c \right]$$

or

$$\eta' = \frac{\tan \phi}{\tan(\phi + \gamma)} \frac{1}{1 + \frac{w_c}{J/\pi}} \quad (12)$$

In equation (12) the first term is the profile efficiency of a blade element, and the second term is the induced efficiency of a blade element. Therefore,

$$\eta_o' = \frac{\tan \phi}{\tan(\phi + \gamma)} \quad (13)$$

$$\eta_i' = \frac{1}{1 + \frac{w_c}{J/\pi}} \quad (14)$$

Both rotational and axial losses are taken into account by the factor w_c in the expression for induced efficiency.

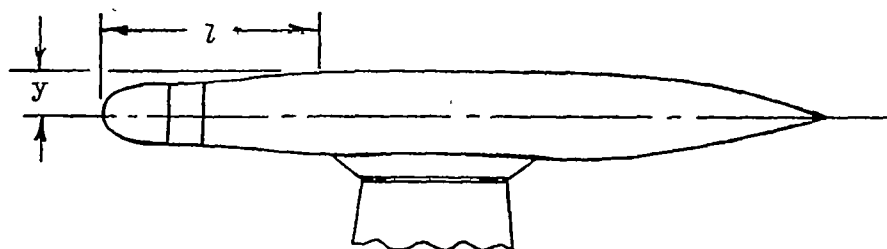
REFERENCES

1. Stack, John, Draley, Eugene C., Delano, James B., and Feldman, Lewis: Investigation of the NACA 4-(3)(08)-03 and NACA 4-(3)(08)-045 Two-Blade Propellers at Forward Mach Numbers to 0.725 To Determine the Effects of Compressibility and Solidity on Performance. NACA Rep. 999, 1950. (Supersedes NACA ACR's 4A10 and 4B16.)
2. Delano, James B.: Investigation of the NACA 4-(5)(08)-03 and NACA 4-(10)(08)-03 Two-Blade Propellers at Forward Mach Numbers to 0.725 To Determine the Effects of Camber and Compressibility on Performance. NACA Rep. 1012, 1951. (Supersedes NACA ACR L5F15.)
3. Moore, Charles S., Biermann, Arnold E., and Voss, Fred: The NACA Balanced-Diaphragm Dynamometer-Torque Indicator. NACA RB 4C28, 1944.
4. Weld, LeRoy D.: Theory of Errors and Least Squares. The Macmillan Co., 1937.
5. Hartman, Edwin P., and Feldman, Lewis: Aerodynamic Problems in the Design of Efficient Propellers. NACA ACR, Aug. 1942.
6. Glauert, H.: The Elements of Aerofoil and Airscrew Theory. American ed., The Macmillan Co., 1943, pp. 222-226.
7. Cooper, Morton: Comparison of Tests of a 4-Foot-Diameter Propeller in the Langley 8-Foot and 16-Foot High-Speed Tunnels. NACA ACR L5H31, 1946.
8. Crigler, John L., and Talkin, Herbert W.: Charts for Determining Propeller Efficiency. NACA ACR L4I29, 1944.
9. Maynard, Julian D.: Aerodynamic Characteristics at High Speeds of Full-Scale Propellers Having Different Shank Designs. NACA RM L6L27a, 1947.
10. Delano, James B., and Carmel, Melvin M.: Effect of Shank Design on Propeller Performance at High Speeds. NACA ARR L6D23, 1946.
11. Hammack, Jerome B.: Investigation of Thrust Losses Due to Shanks of a Flared-Shank Two-Blade Propeller on a Slender-Nose Airplane. NACA TN 1414, 1947.
12. Gilman, Jean, Jr.: Wind-Tunnel Tests and Analysis of Three 10-Foot-Diameter Three-Blade Tractor Propellers Differing in Pitch Distribution. NACA ARR L6E22, 1946.

13. Lindsey, W. F., Stevenson, D. B., and Daley, Bernard N.: Aerodynamic Characteristics of 24 NACA 16-Series Airfoils at Mach Numbers Between 0.3 and 0.8. NACA TN 1546, 1948.
14. Crigler, John L.: Comparison of Calculated and Experimental Propeller Characteristics for Four-, Six-, and Eight-Blade Single-Rotating Propellers. NACA ACR 4304, 1944.

TABLE I

ORDINATES FOR THE DYNAMOMETER-FAIRING PROFILE



l , in.	Radius, y , in.	l , in.	Radius, y , in.
0	0	88.000	18.00
.563	3.30	188.750	18.00
1.688	5.34	190.500	17.99
3.313	7.11	194.500	17.97
4.948	8.44	198.500	17.93
6.563	9.37	202.500	17.82
8.188	10.08	206.500	17.68
9.813	10.64	210.500	17.52
13.063	11.46	214.500	17.30
16.313	12.04	218.500	17.04
19.563	12.46	222.500	16.75
22.813	12.79	226.500	16.40
26.063	12.98	230.500	16.01
28.000	13.00	234.500	15.59
42.250	13.00	238.500	15.09
44.000	13.03	242.500	14.52
48.000	13.24	246.500	13.92
52.000	13.68	250.500	13.26
56.000	14.22	254.500	12.52
60.000	14.83	258.500	11.77
64.000	15.50	262.500	10.94
68.000	16.12	266.500	10.03
72.000	16.70	270.500	9.04
76.000	17.17	273.125	8.31
80.000	17.50	303.000	.25
84.000	17.80		

TABLE II

RANGE OF BLADE ANGLE AND ROTATIONAL SPEED
FOR NACA 10-(3)(08)-03 PROPELLER TESTS

Figure	Rotational speed, rpm	Blade angle at 0.75 radius, $\beta_{0.75R}$, deg							
19	1,140			30	35	40	45	50	55
20	1,350	20	25	30	35	40	45	50	
21	1,500						45		
22	1,600	20	25	30	35	40	45		
23	2,000	20	25	30	35				
24	2,160	20	25	30					
25	Varied						45		



TABLE III

CALCULATED AND EXPERIMENTAL VALUES OF THRUST COEFFICIENT,
POWER COEFFICIENT, AND EFFICIENCY FOR THE TWO-BLADE
NACA 10-(3)(08)-03 PROPELLER

$\beta_{0.75R}$ deg	J	Value	C_T	C_P	η
30	1.18	Calculated	0.0448	0.0584	0.905
		Experimental	.0450	.0583	.910
45	2.20	Calculated	.0447	.1055	.932
		Experimental	.0426	.1014	.924
55	3.22	Calculated	.0579	.2048	.910
		Experimental	.0568	.2010	.910





Figure 1.- Propeller dynamometer in test section with tunnel open.

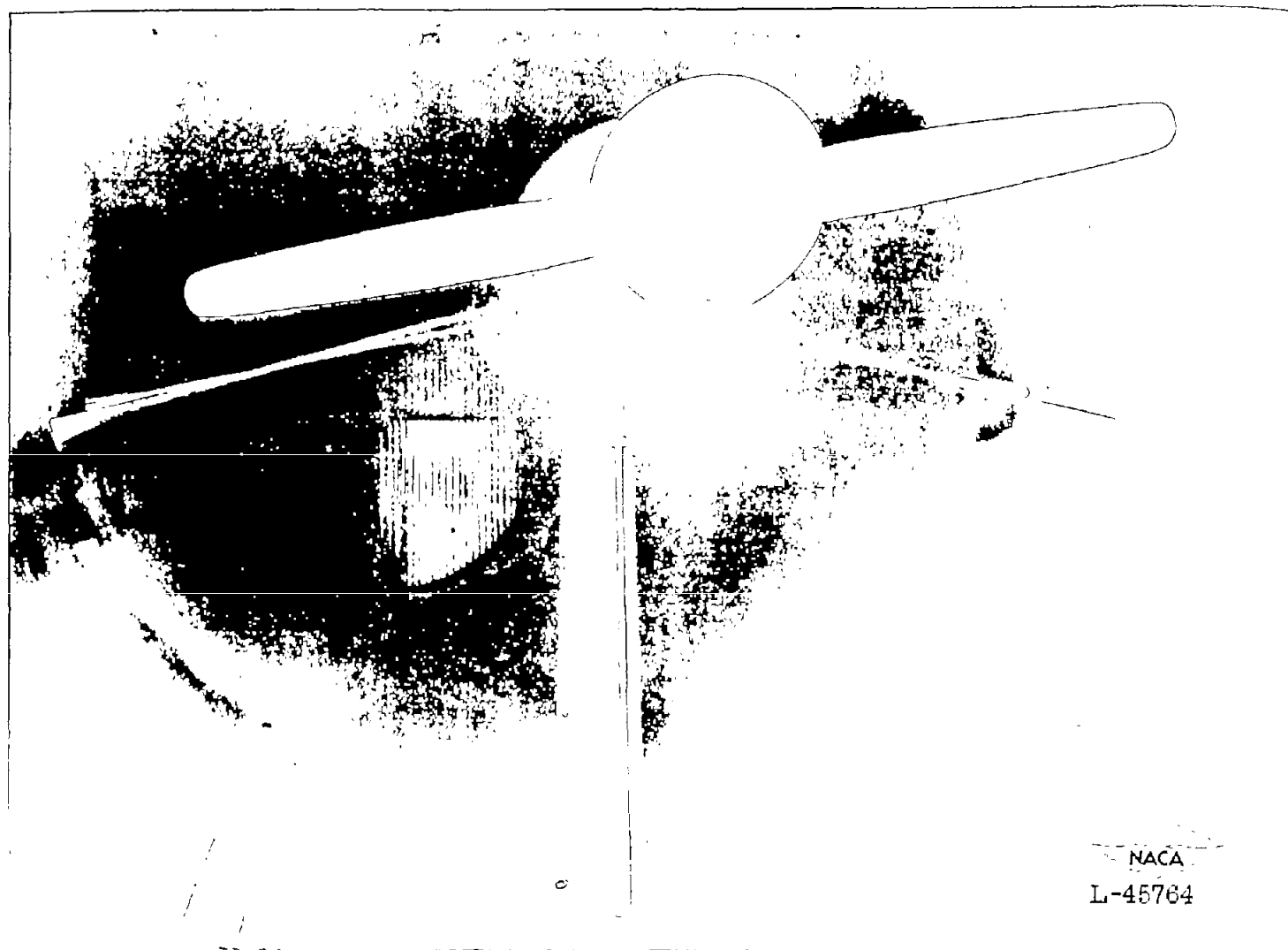


Figure 2.- Propeller dynamometer in test section with tunnel closed.

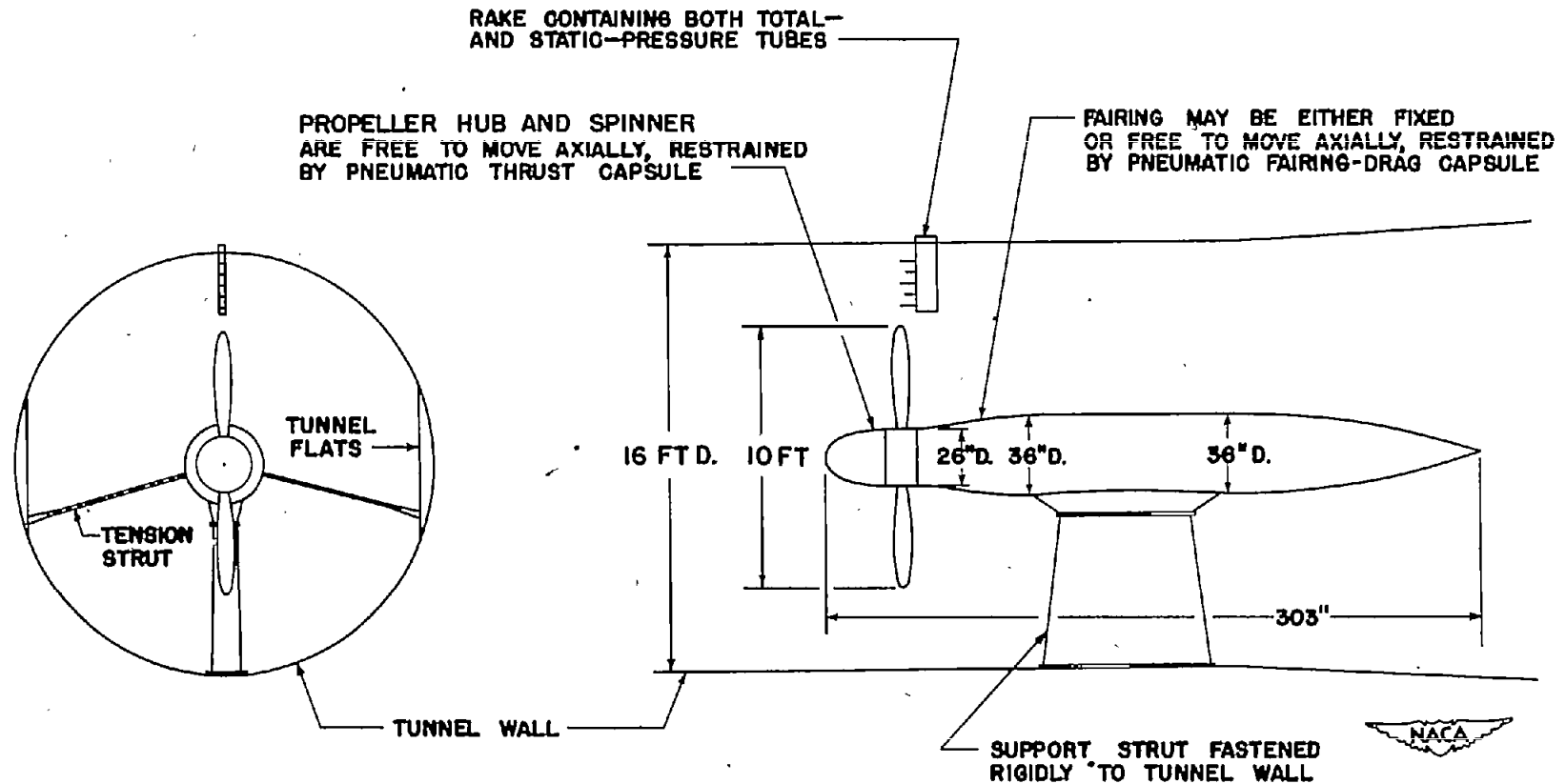


Figure 3.- Configuration of 2,000-horsepower dynamometer for tests of propellers in the Langley 16-foot high-speed tunnel.

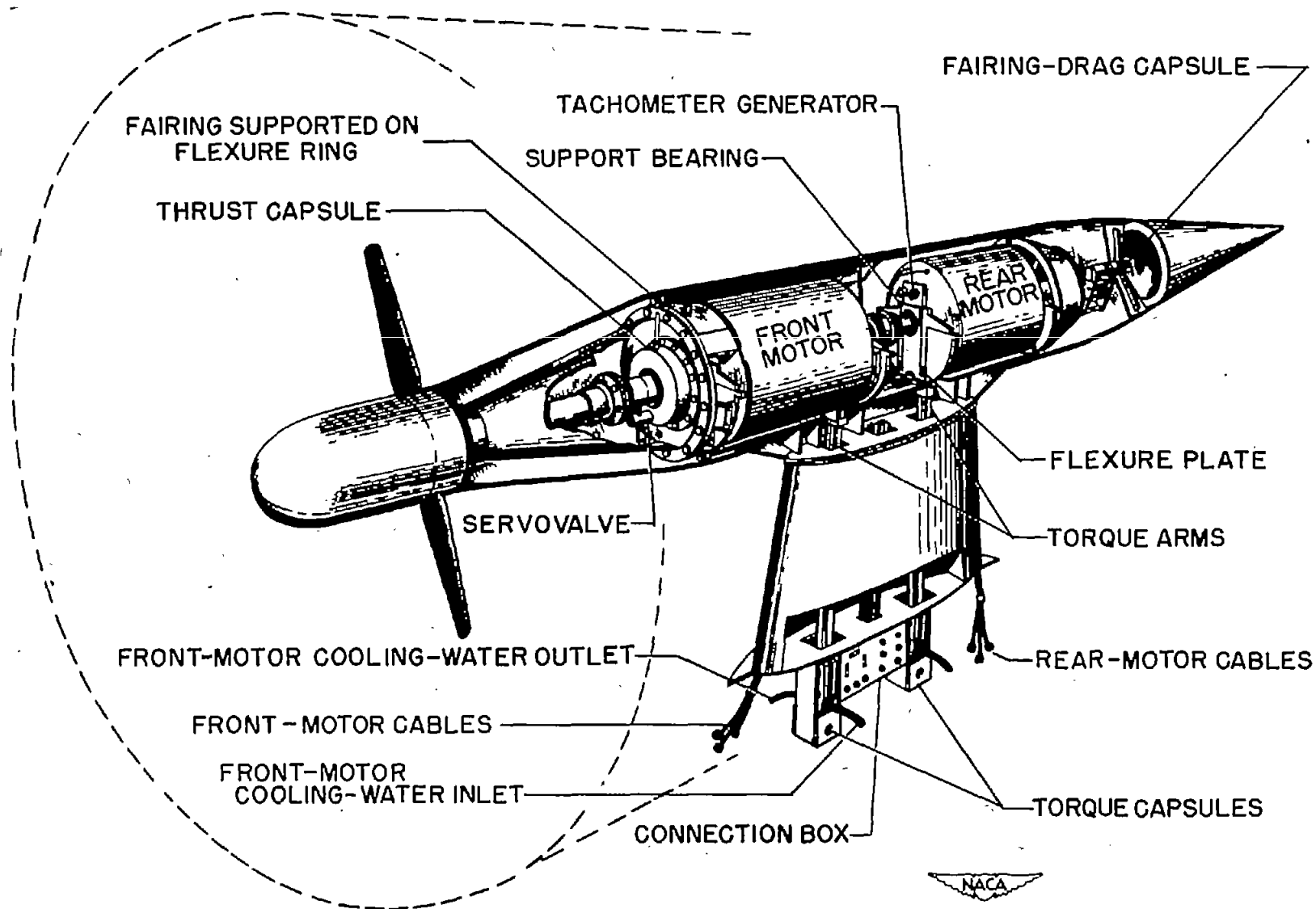


Figure 4.- Cutaway view showing location of various parts in the dynamometer.

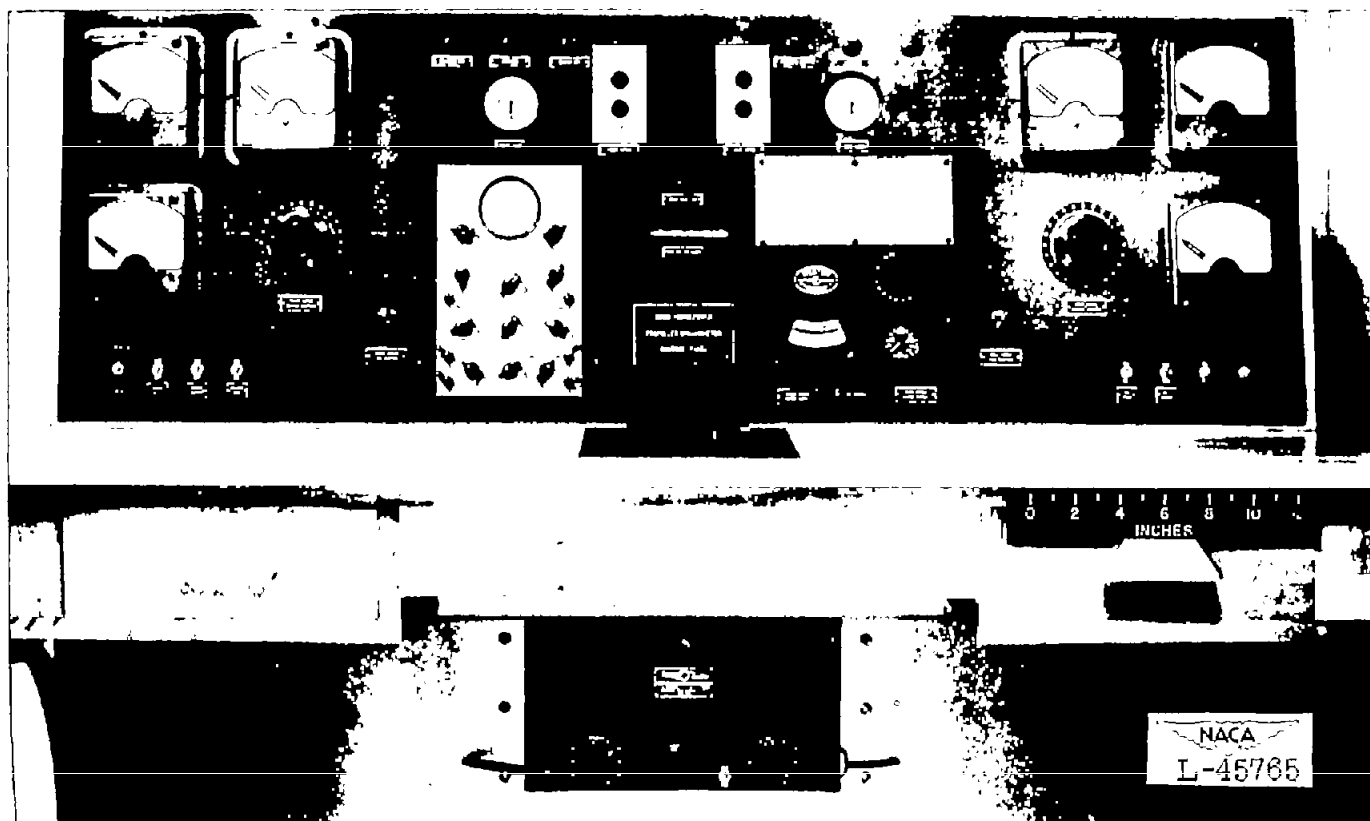


Figure 5.- Control panel for the Langley 2,000-horsepower propeller dynamometer.

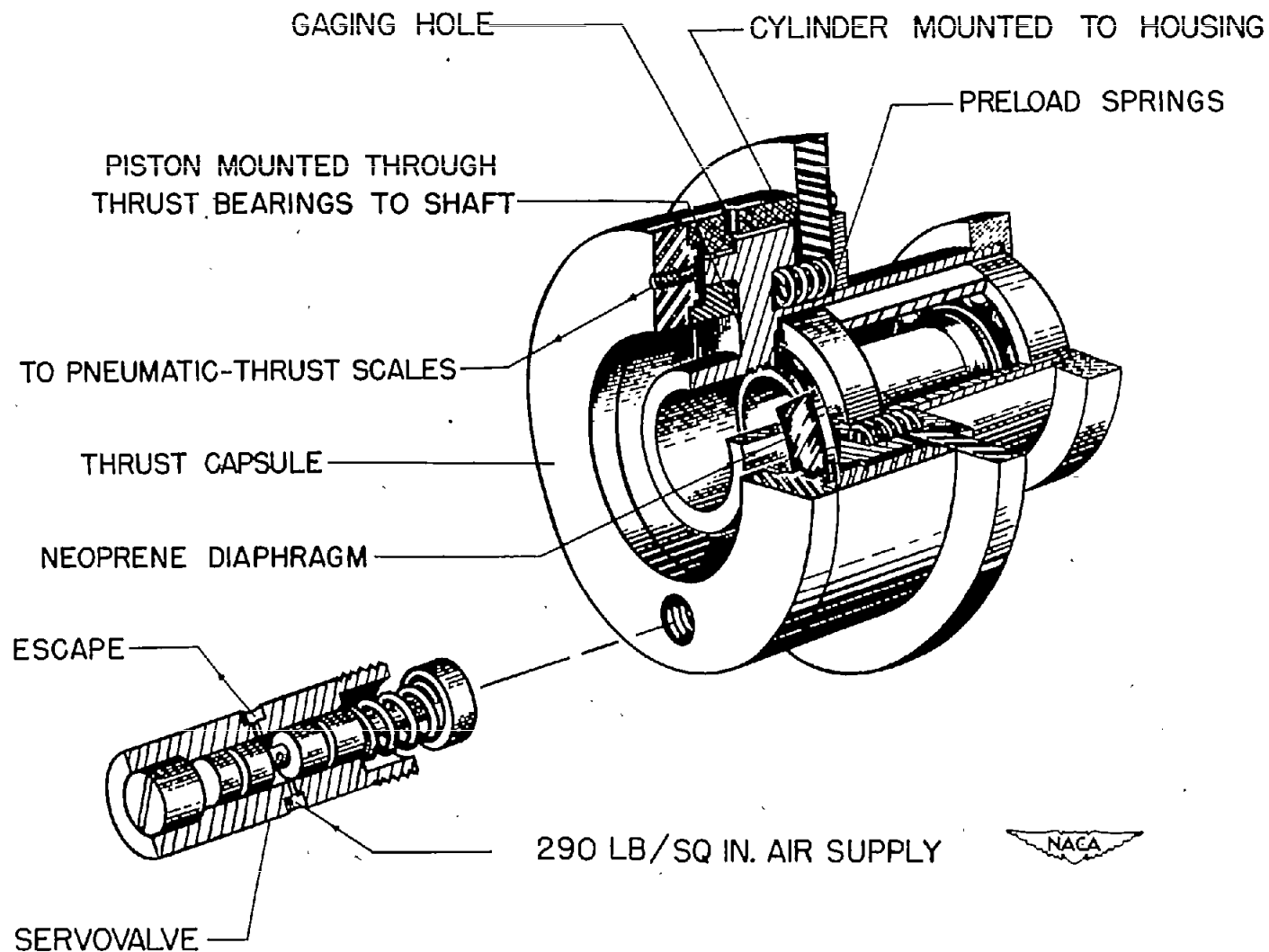


Figure 6.- Cutaway view showing arrangement in thrust capsule and servovalve.

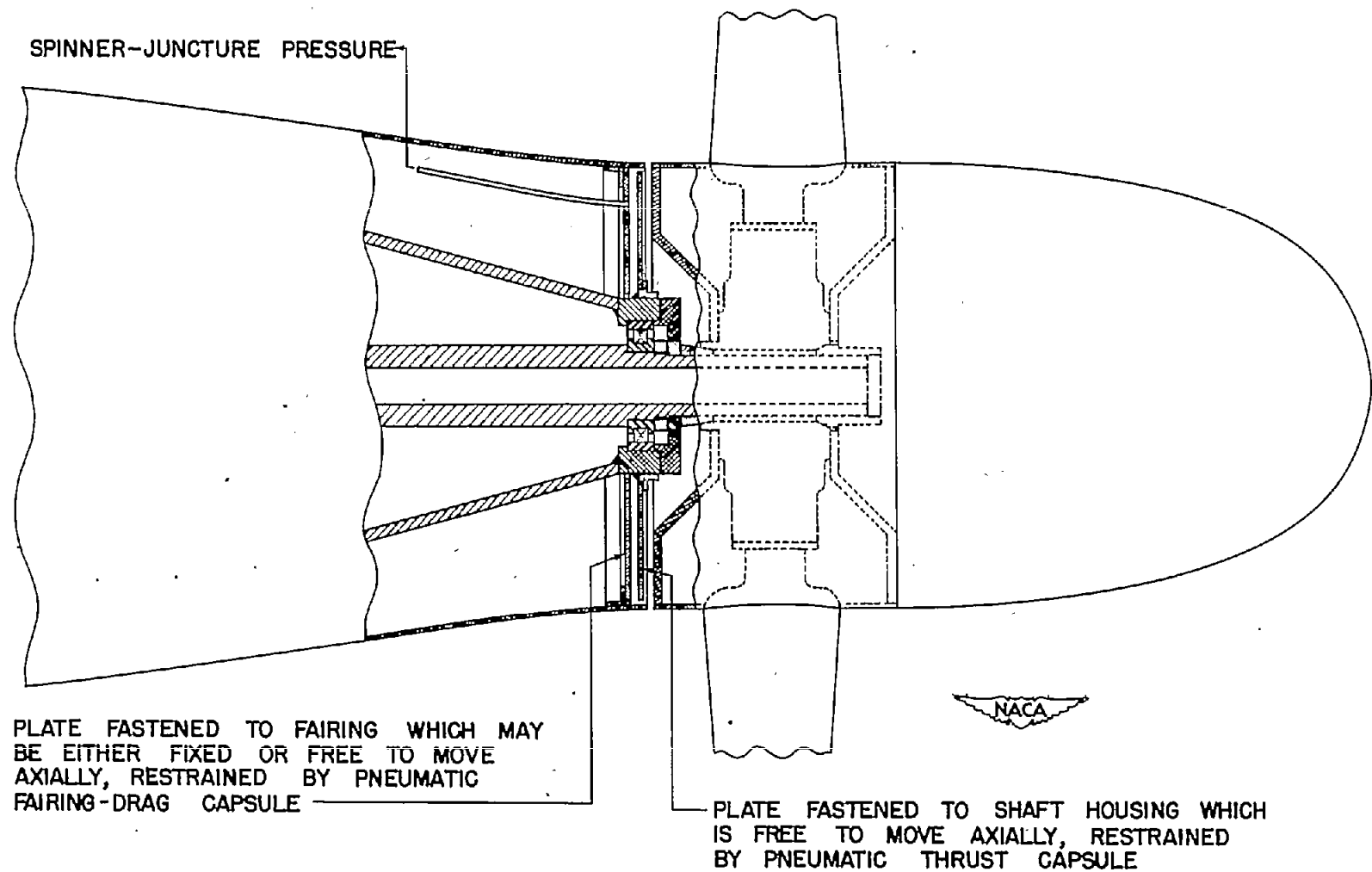


Figure 7.- Cutaway section showing arrangement in nose of propeller dynamometer.



Figure 8.- Pneumatic-pressure scales used for measuring thrust.

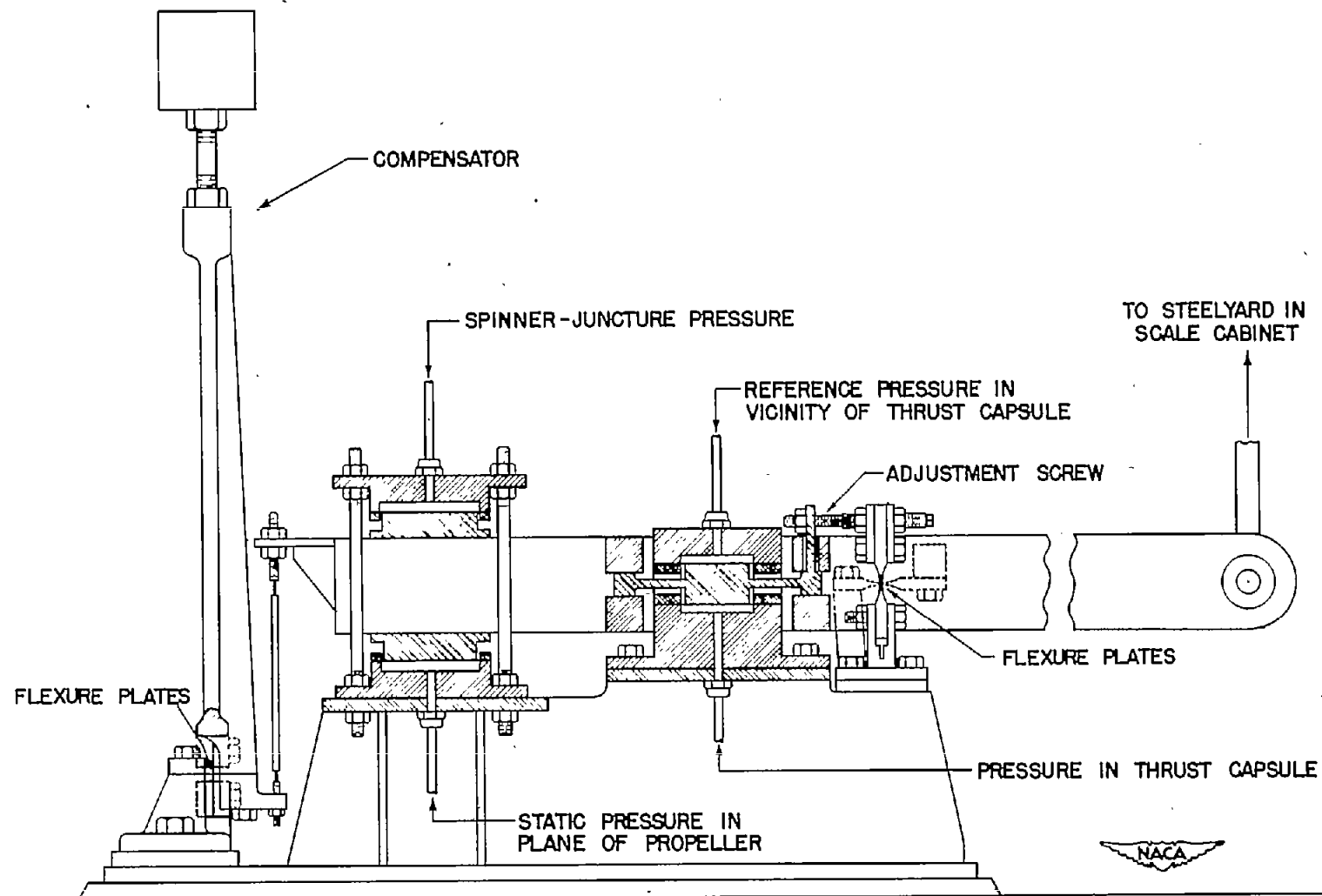


Figure 9.- Device for transferring the thrust pressures into a force on the steelyard in a scale cabinet.

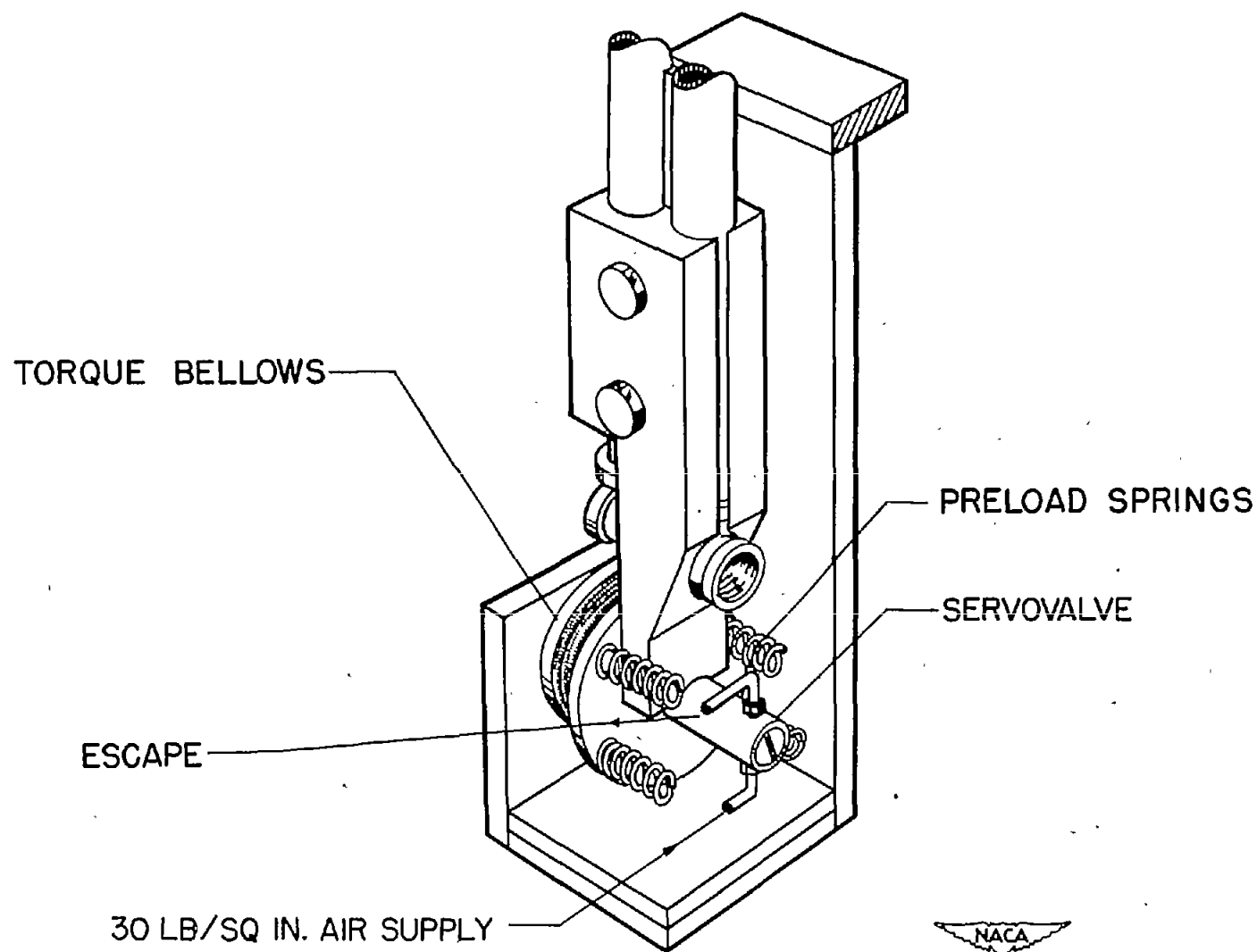


Figure 10.- Cutaway view showing arrangement in one of the torque capsules.

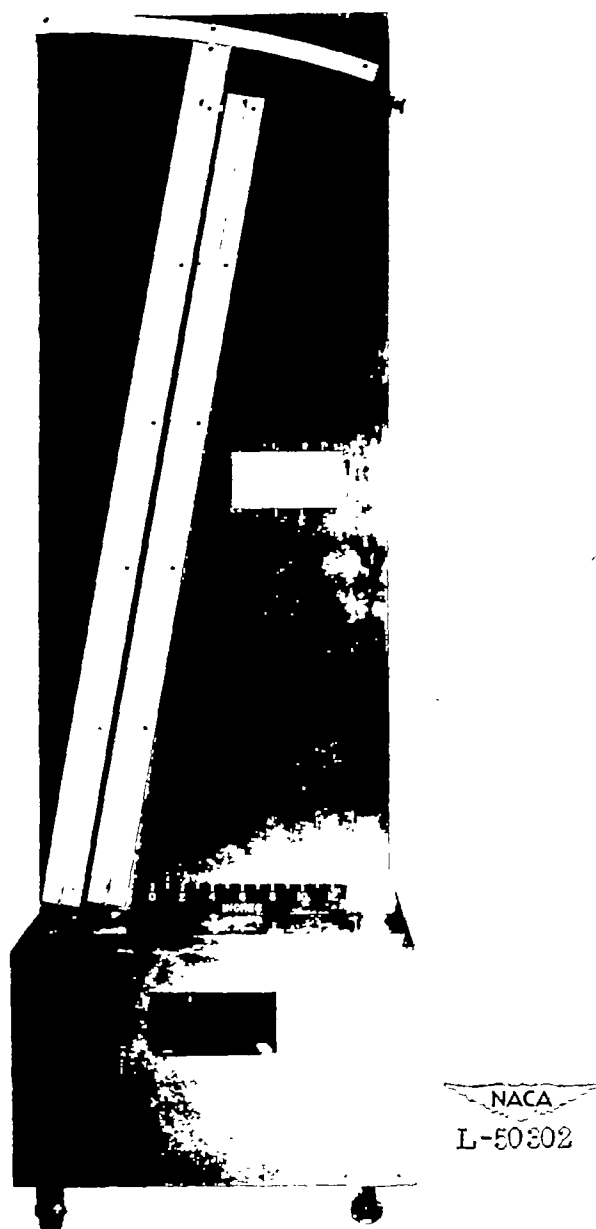


Figure 11.- Mercury manometer used for measuring torque.

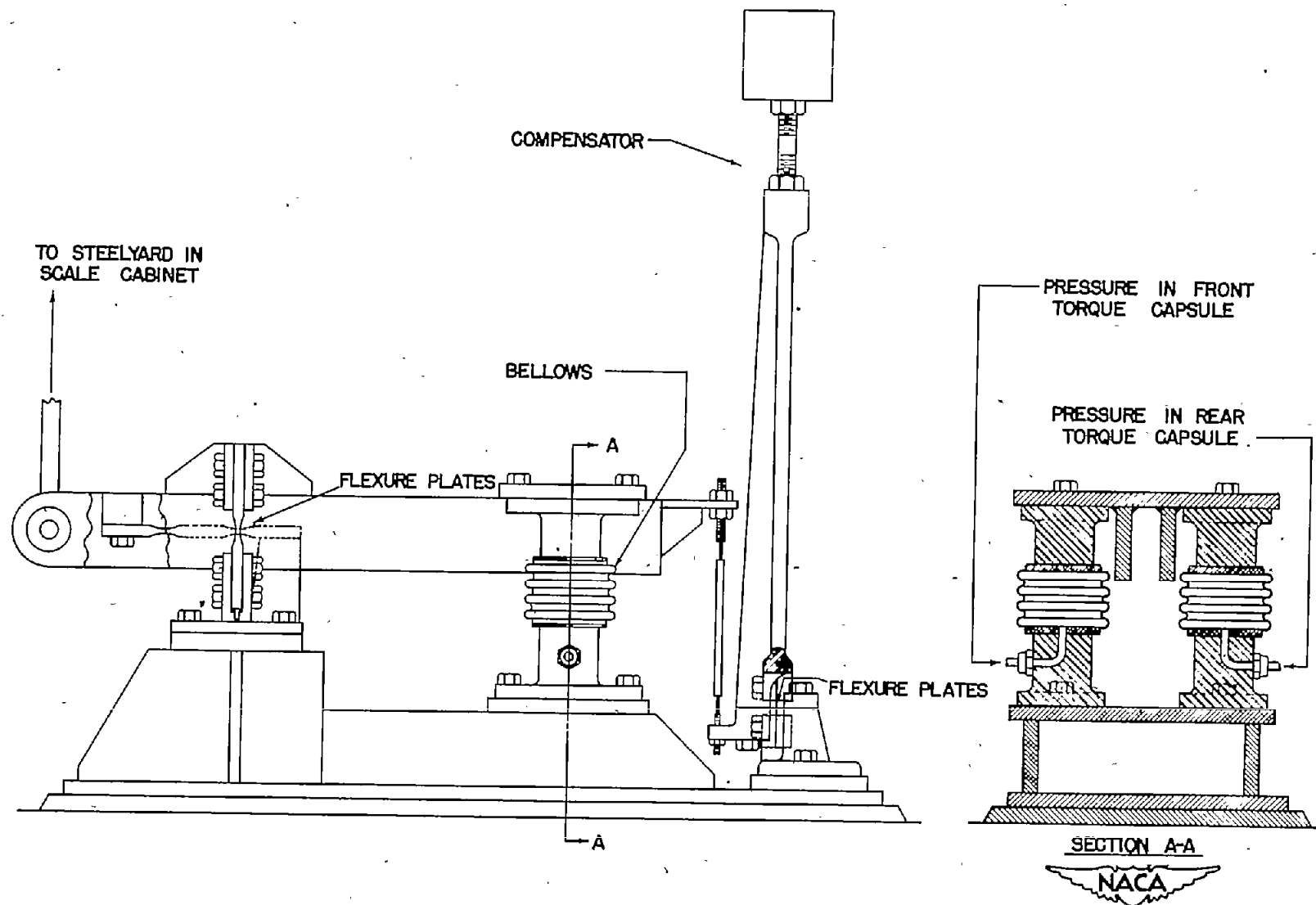


Figure 12.- Device for transferring pressures in the torque capsules into a force on the steelyard in a scale cabinet.

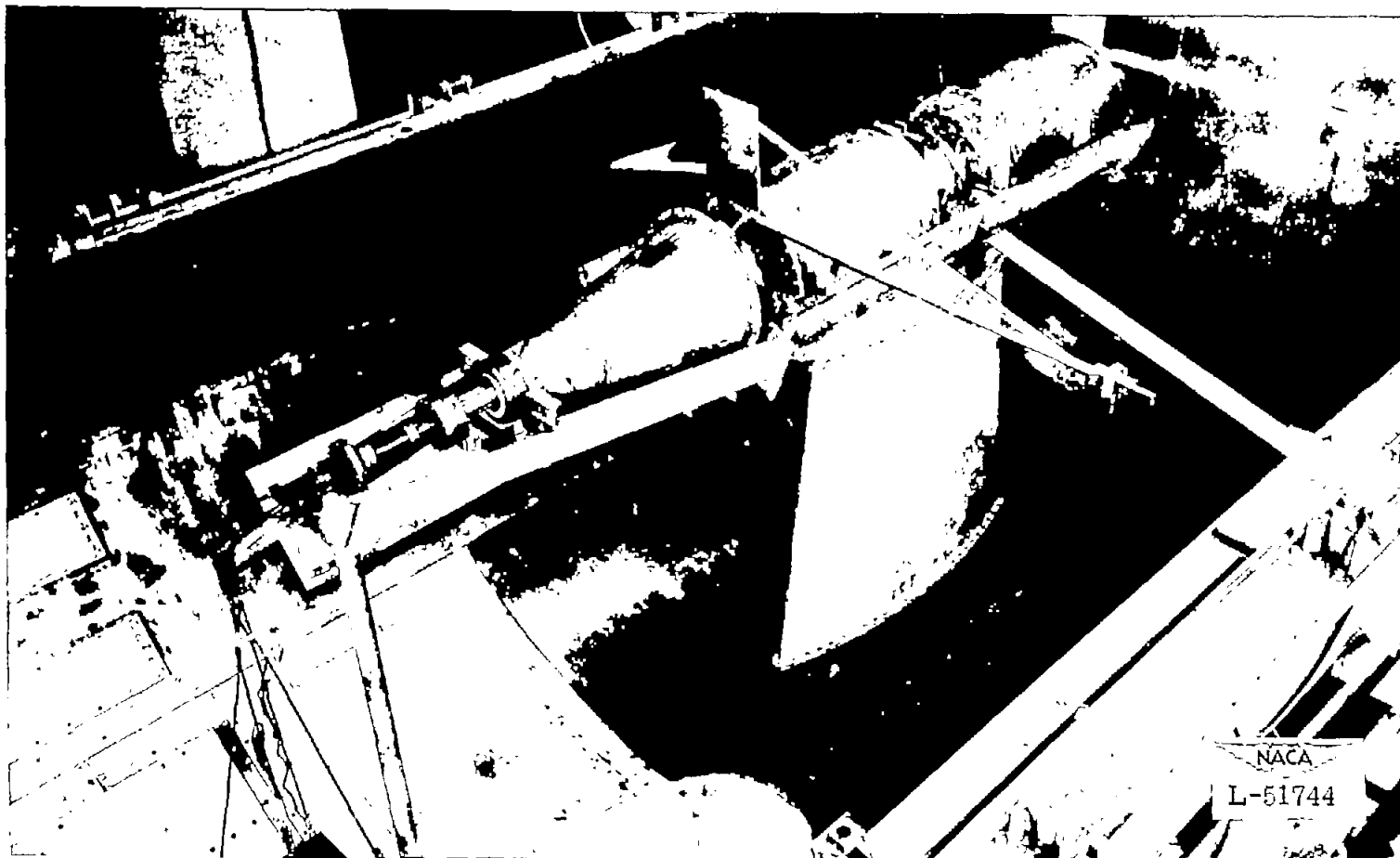


Figure 13.- Equipment used for applying thrust and torque loads in calibrating the Langley 2,000-horsepower propeller dynamometer.

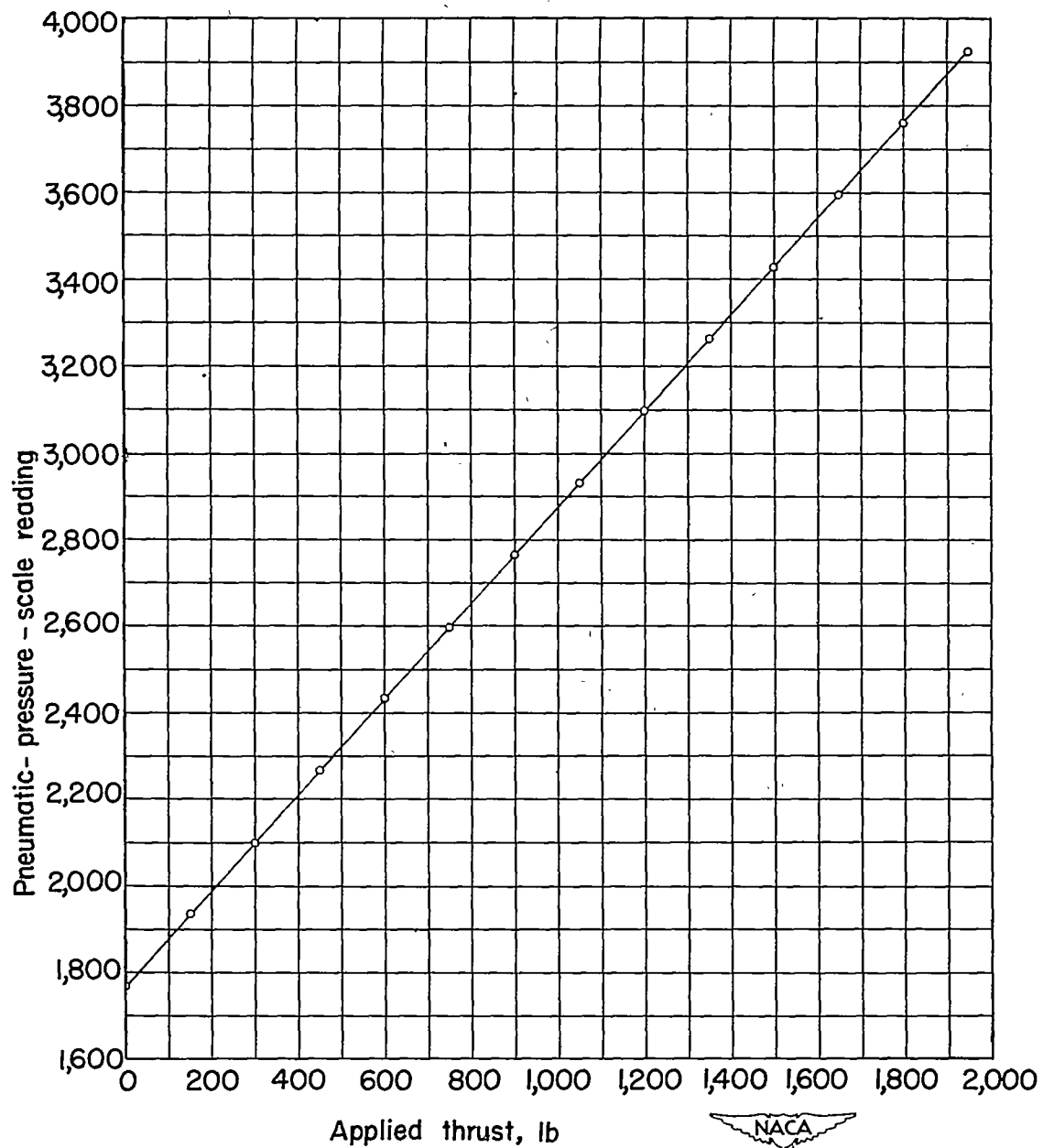


Figure 14.- Sample calibration of thrust capsule.

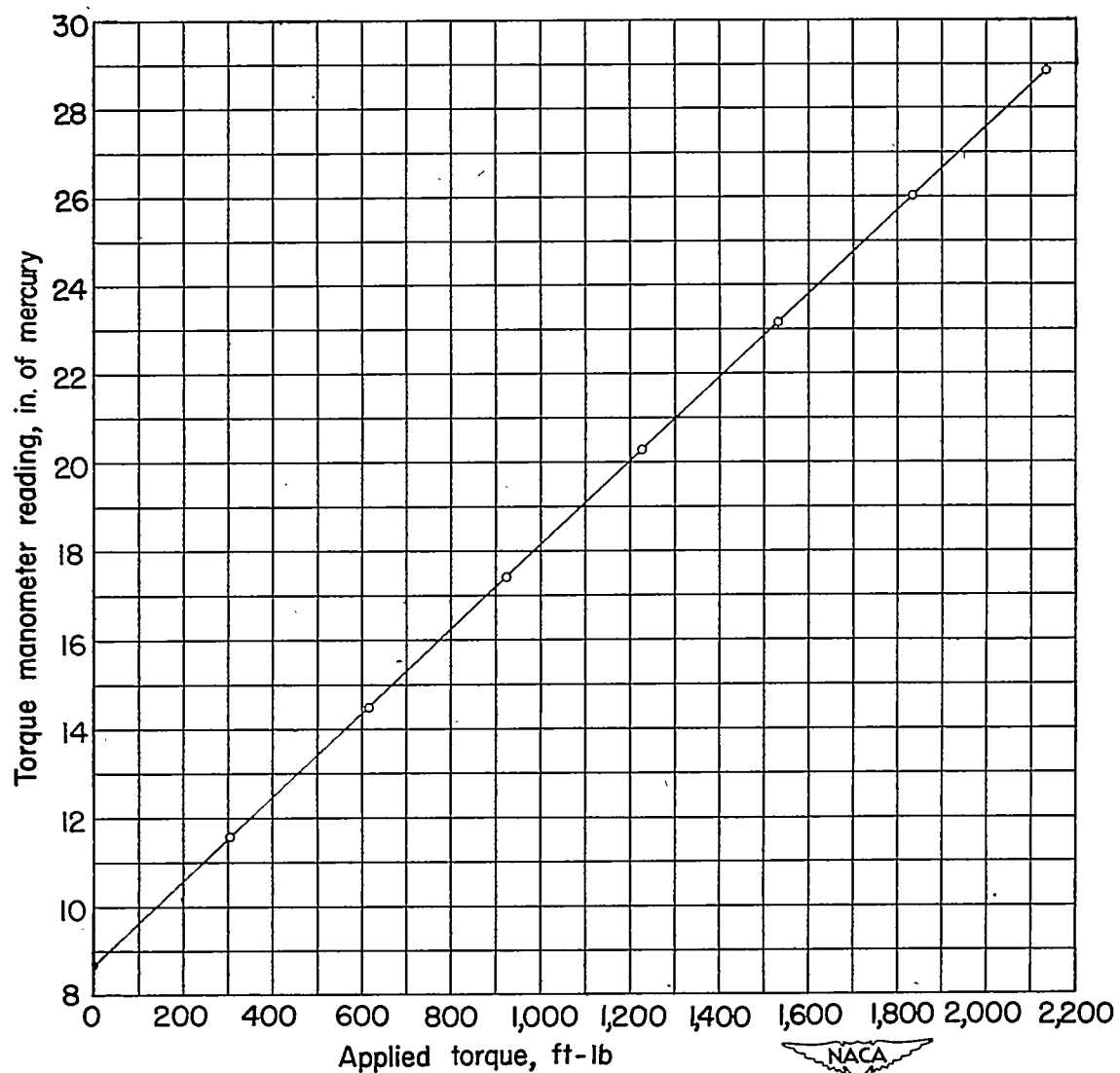


Figure 15.- Sample calibration of rear-motor torque capsule.

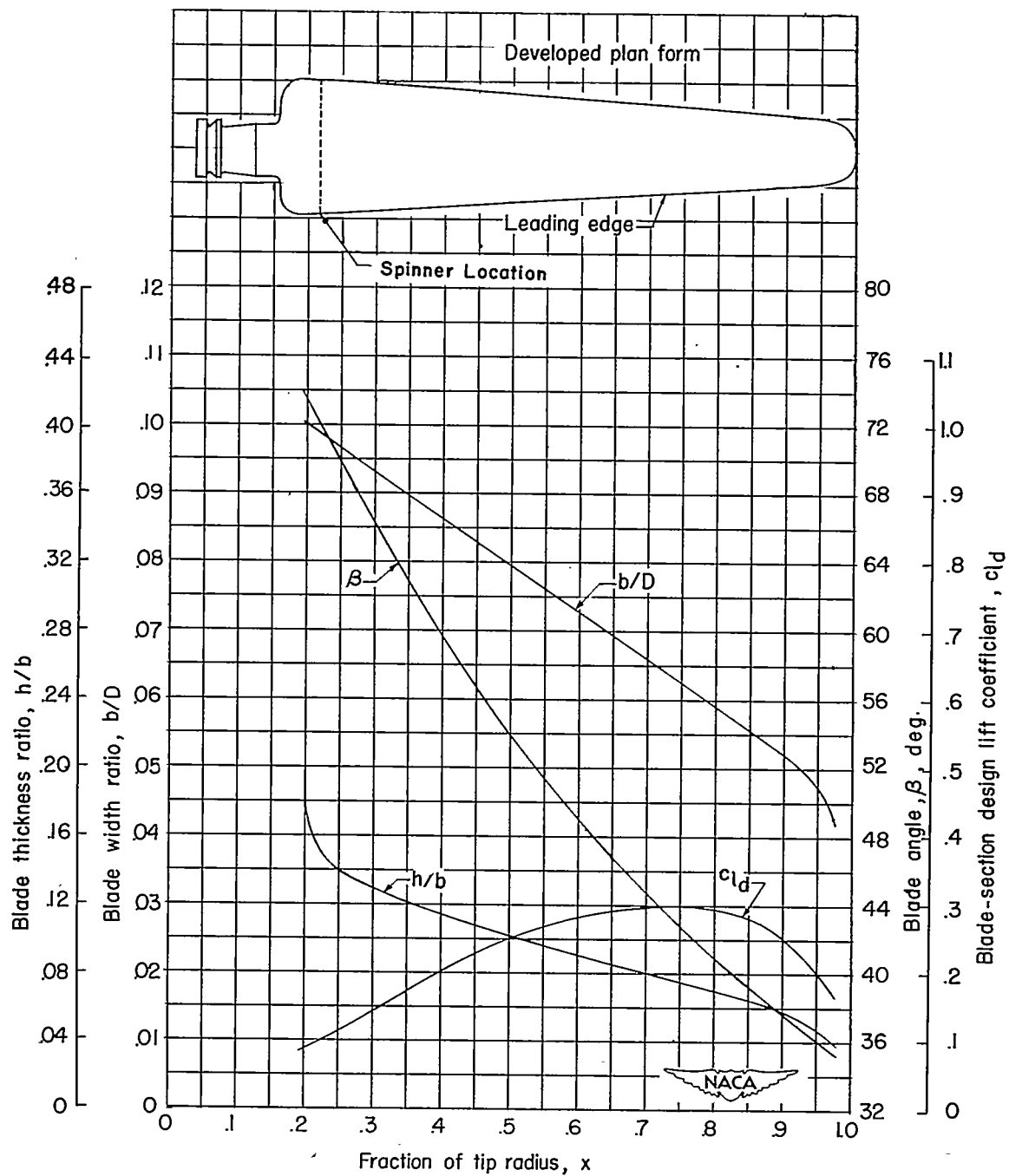


Figure 16.- Blade-form curves for NACA 10-(3)(08)-03 propeller.



Figure 17.- Blade of NACA 10-(3)(08)-03 propeller.

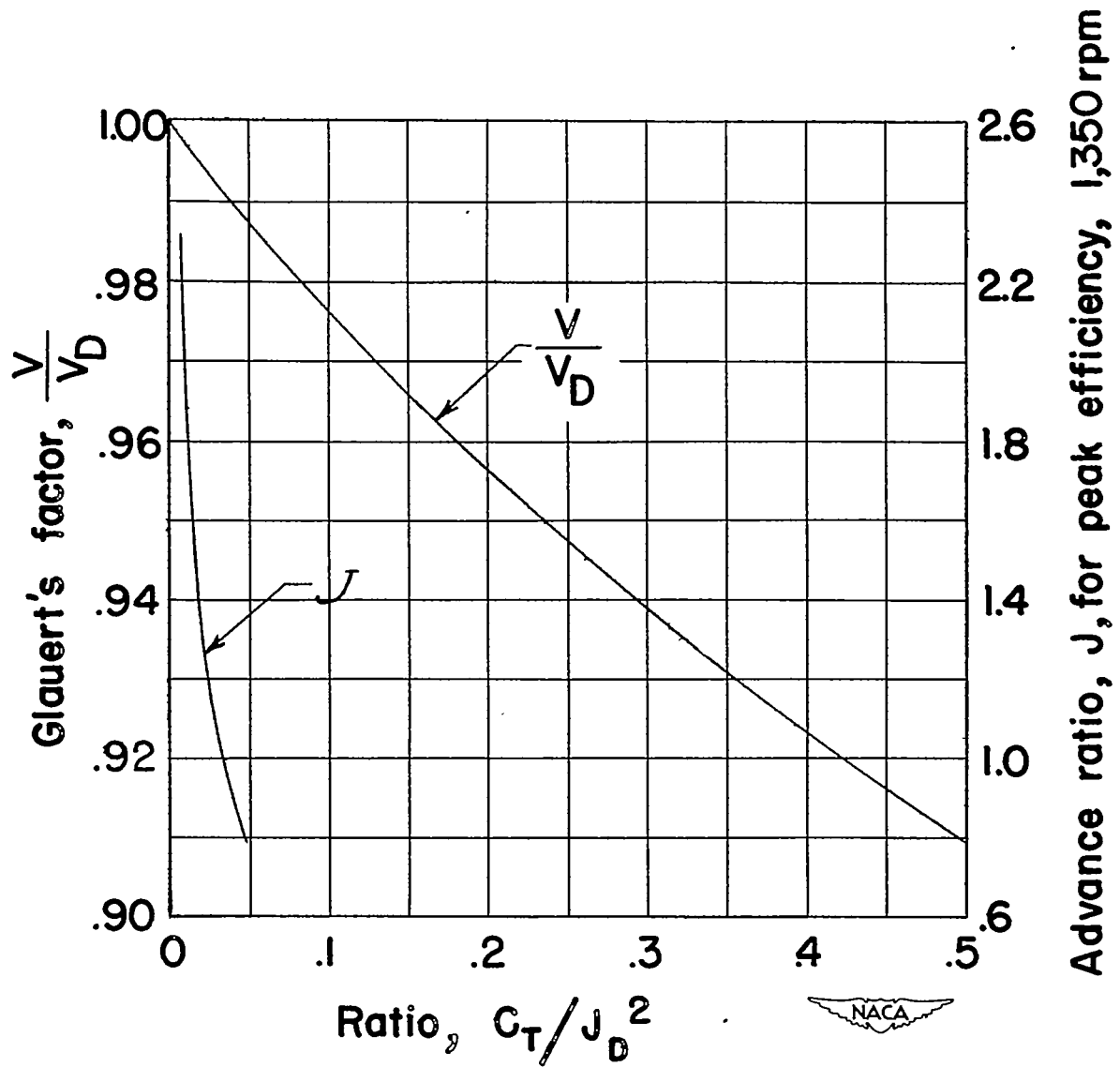
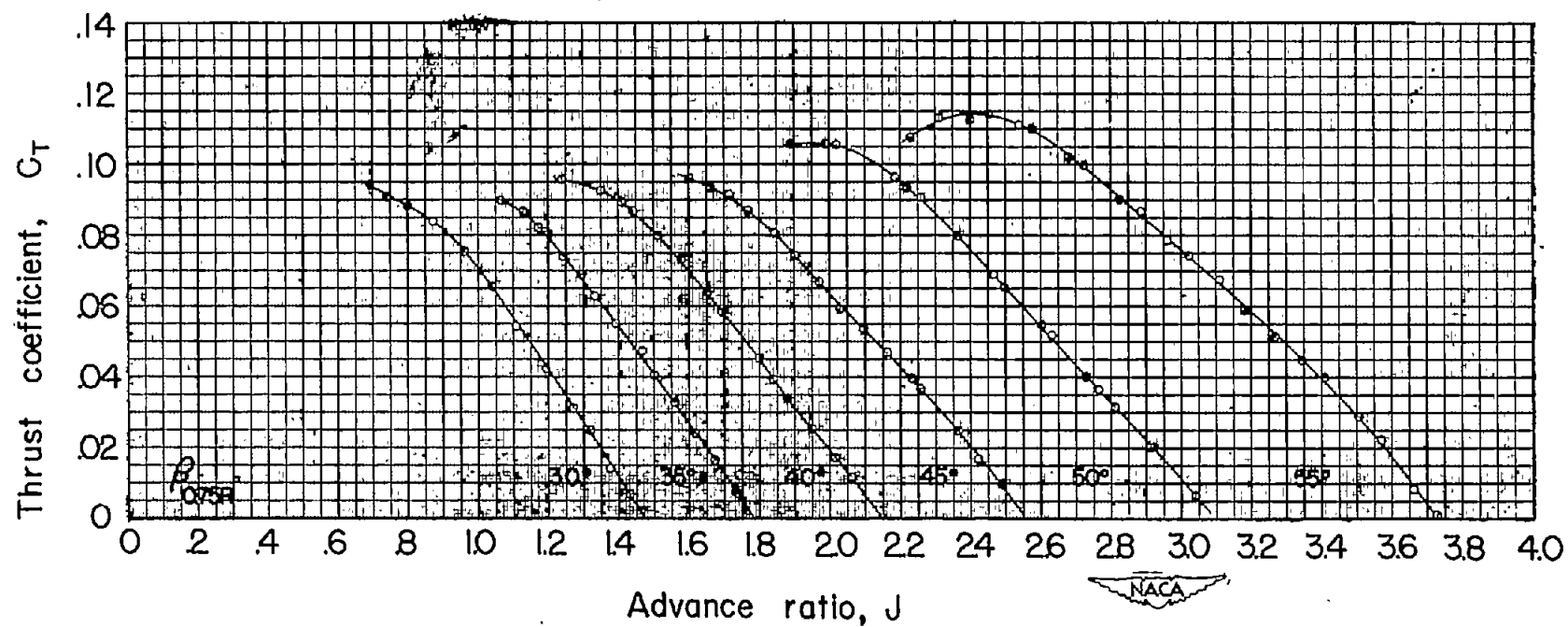
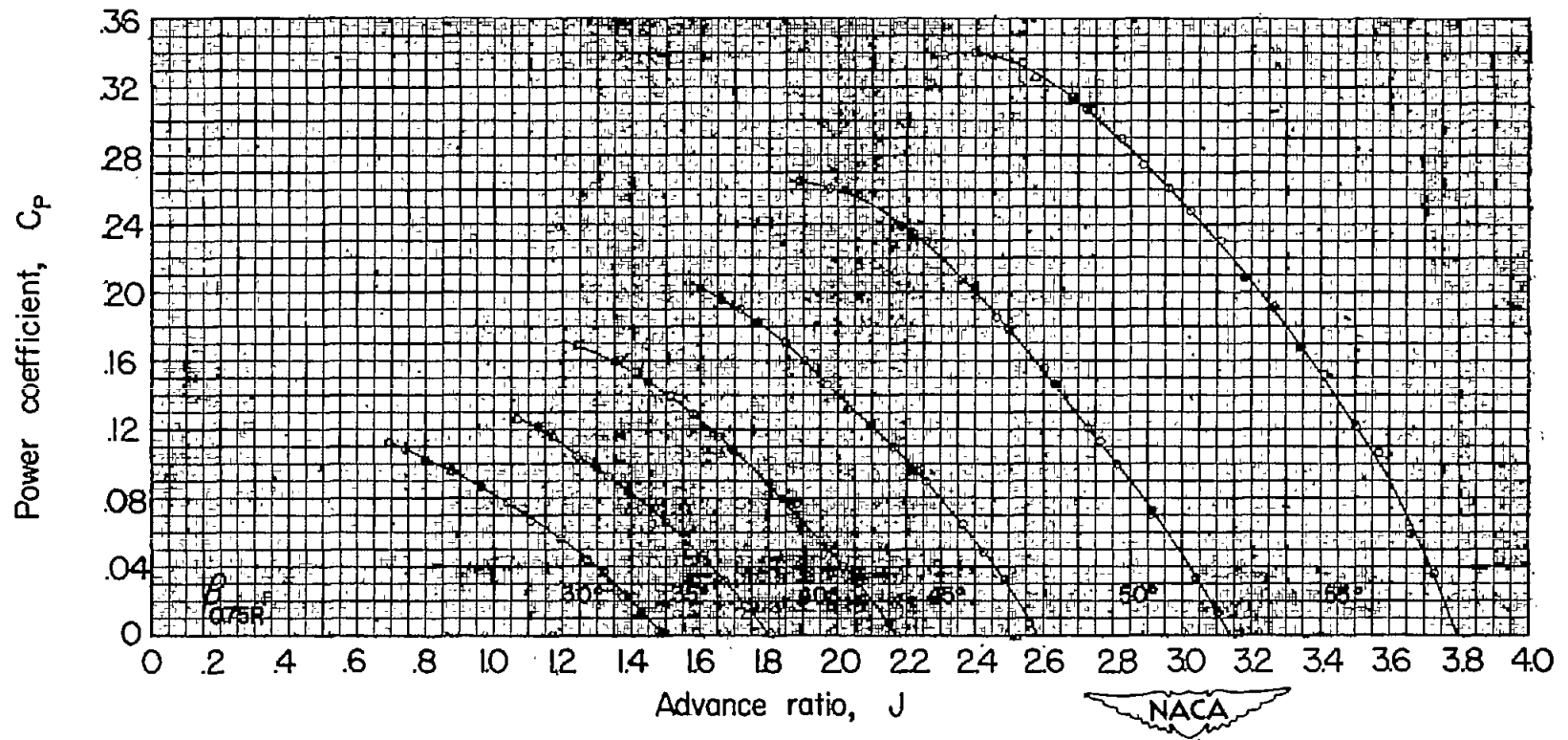


Figure 18.- Glauert's factor for correcting wind-tunnel datum velocity to equivalent free airspeed for a 10-foot-diameter propeller in a closed 16-foot circular jet.



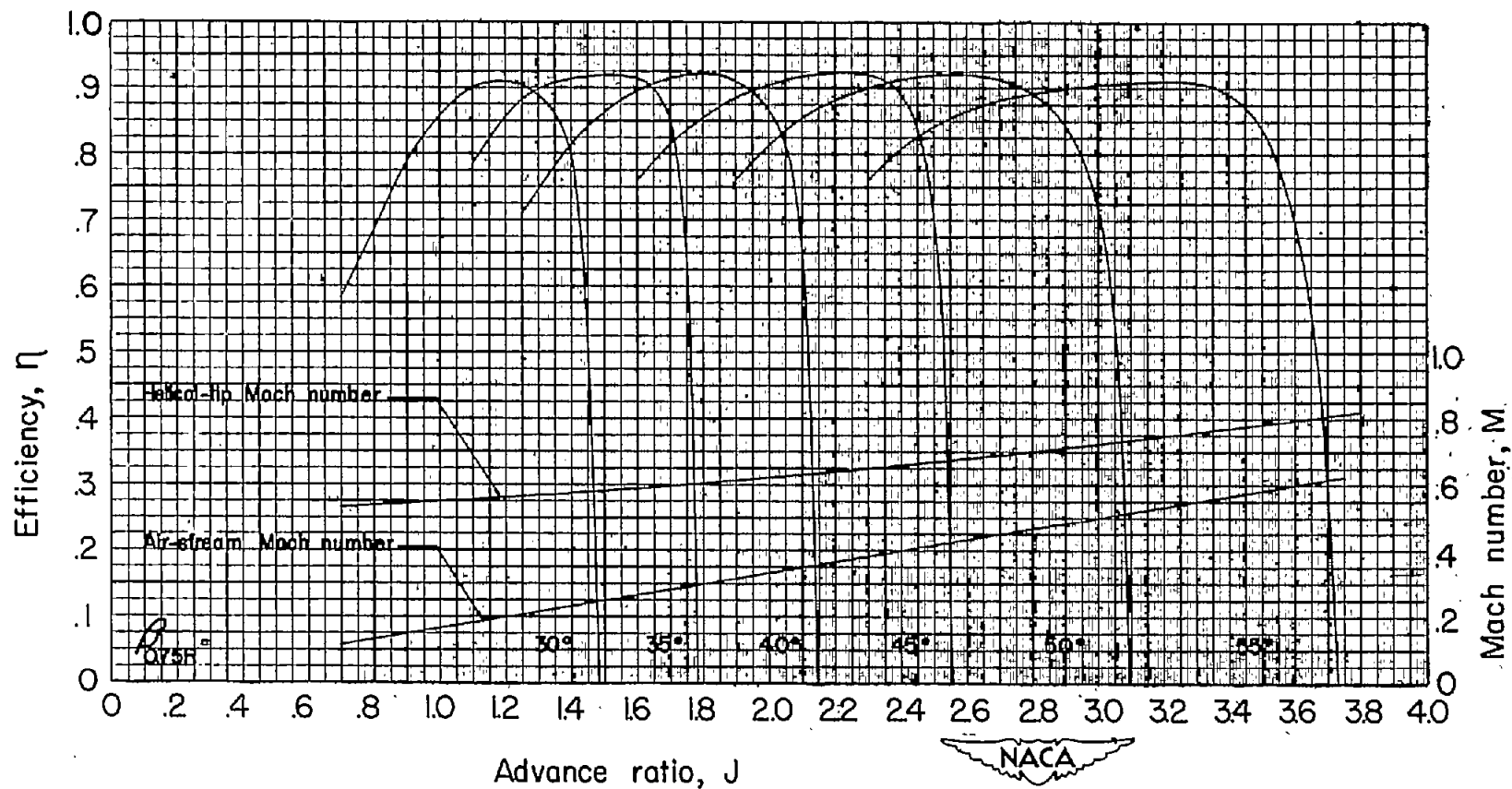
(a) Thrust coefficient.

Figure 19.- Characteristics of NACA 10-(3)(08)-03 propeller. Rotational speed, 1,140 rpm.



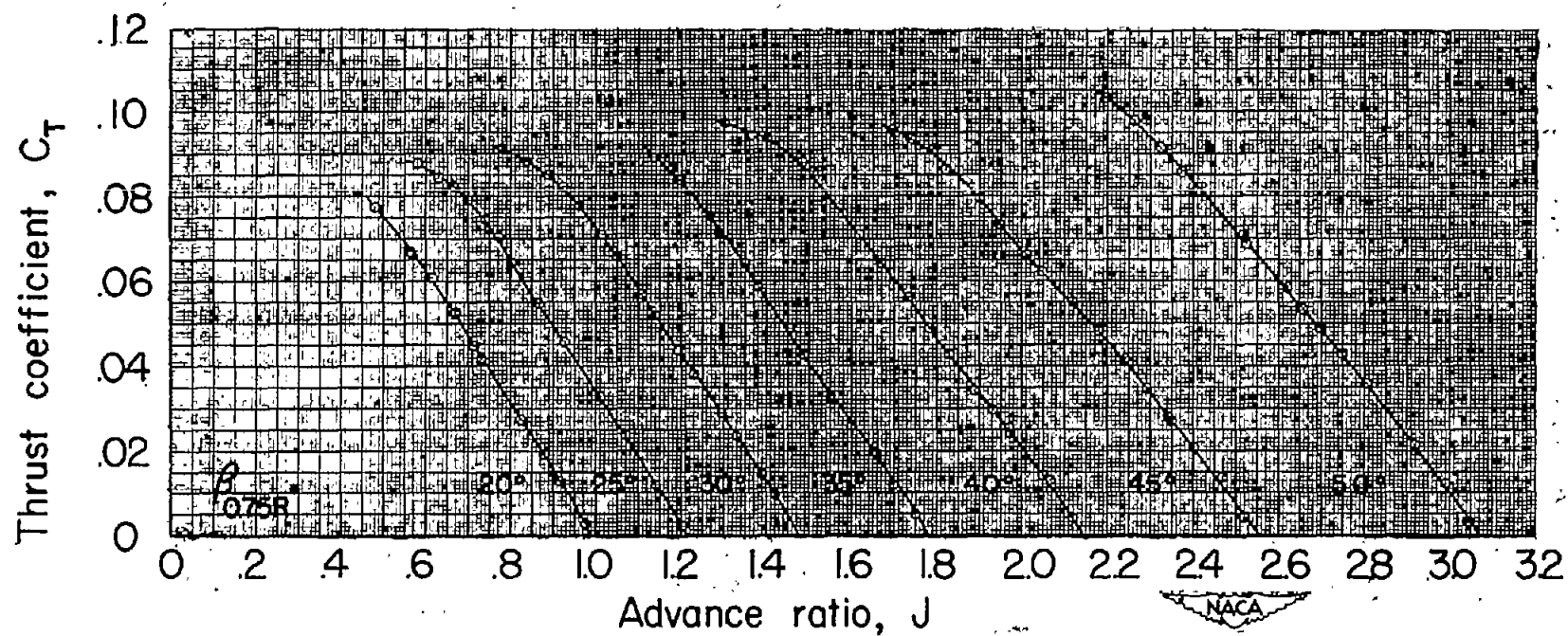
(b) Power coefficient.

Figure 19.- Continued. Rotational speed, 1,140 rpm.



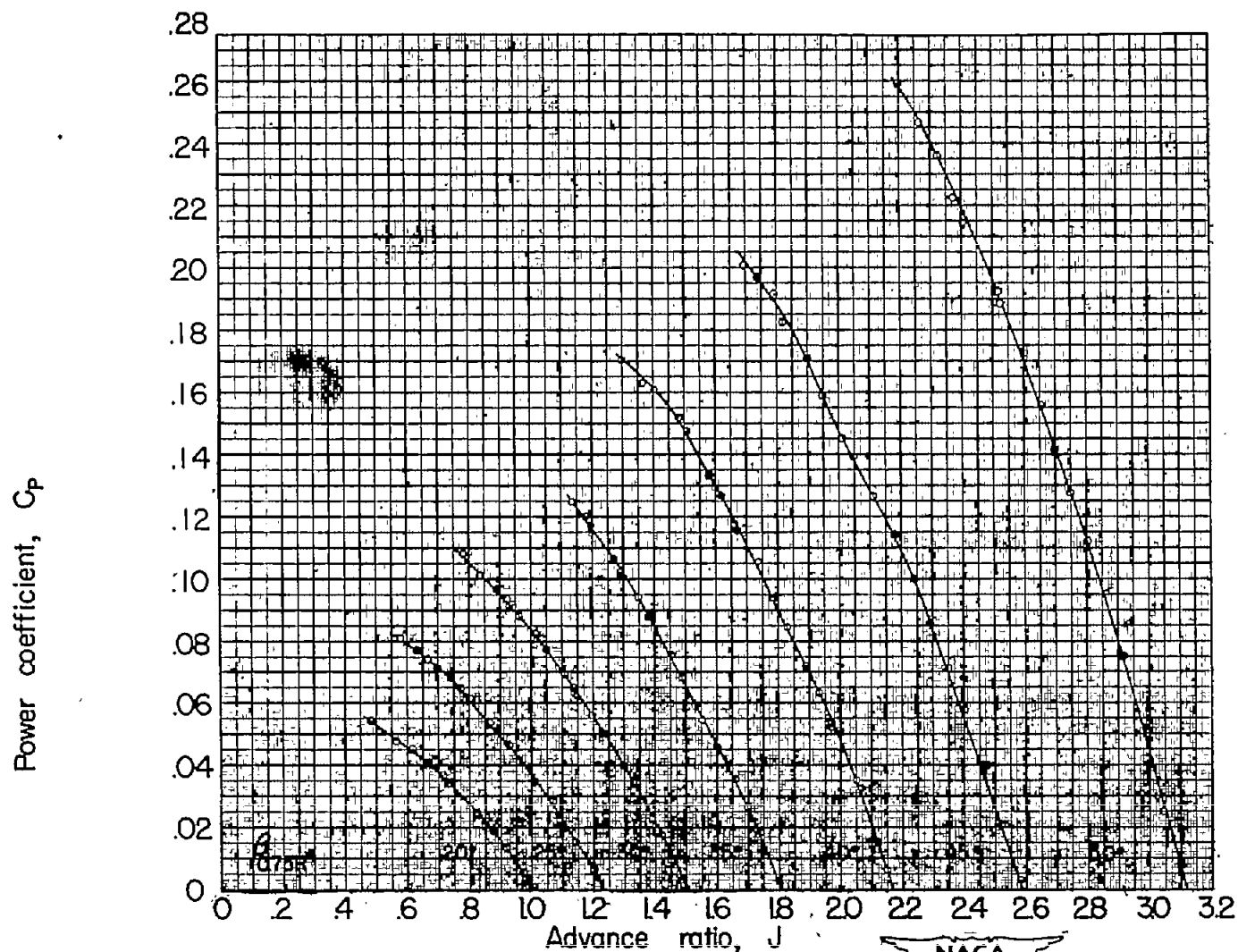
(c) Efficiency.

Figure 19.- Concluded. Rotational speed, 1,140 rpm.



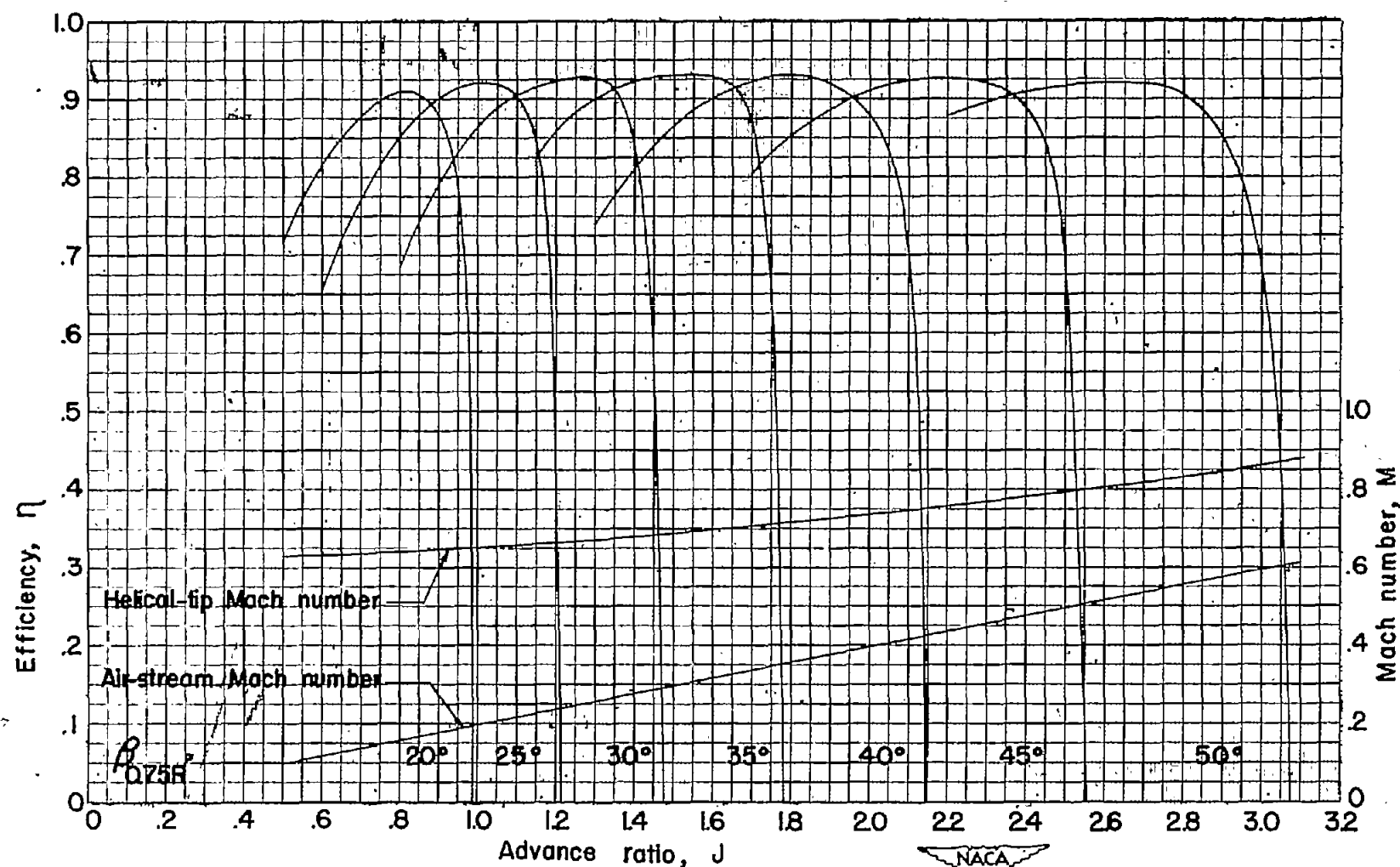
(a) Thrust coefficient.

Figure 20.- Characteristics of NACA 10-(3)(08)-03 propeller. Rotational speed, 1,350 rpm.



(b) Power coefficient.

Figure 20.- Continued. Rotational speed, 1,350 rpm.



(c) Efficiency.

Figure 20.- Concluded. Rotational speed, 1,350 rpm.

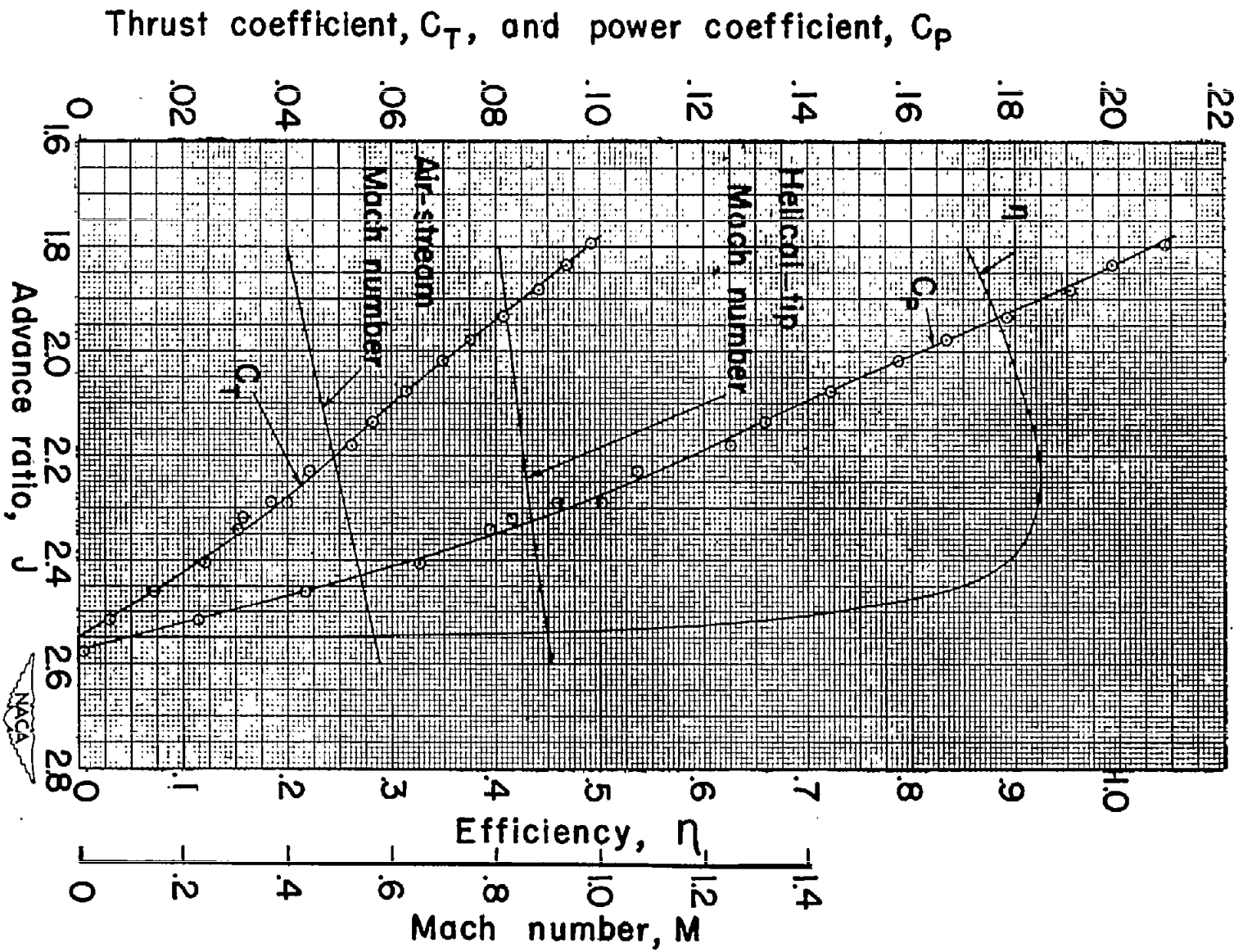
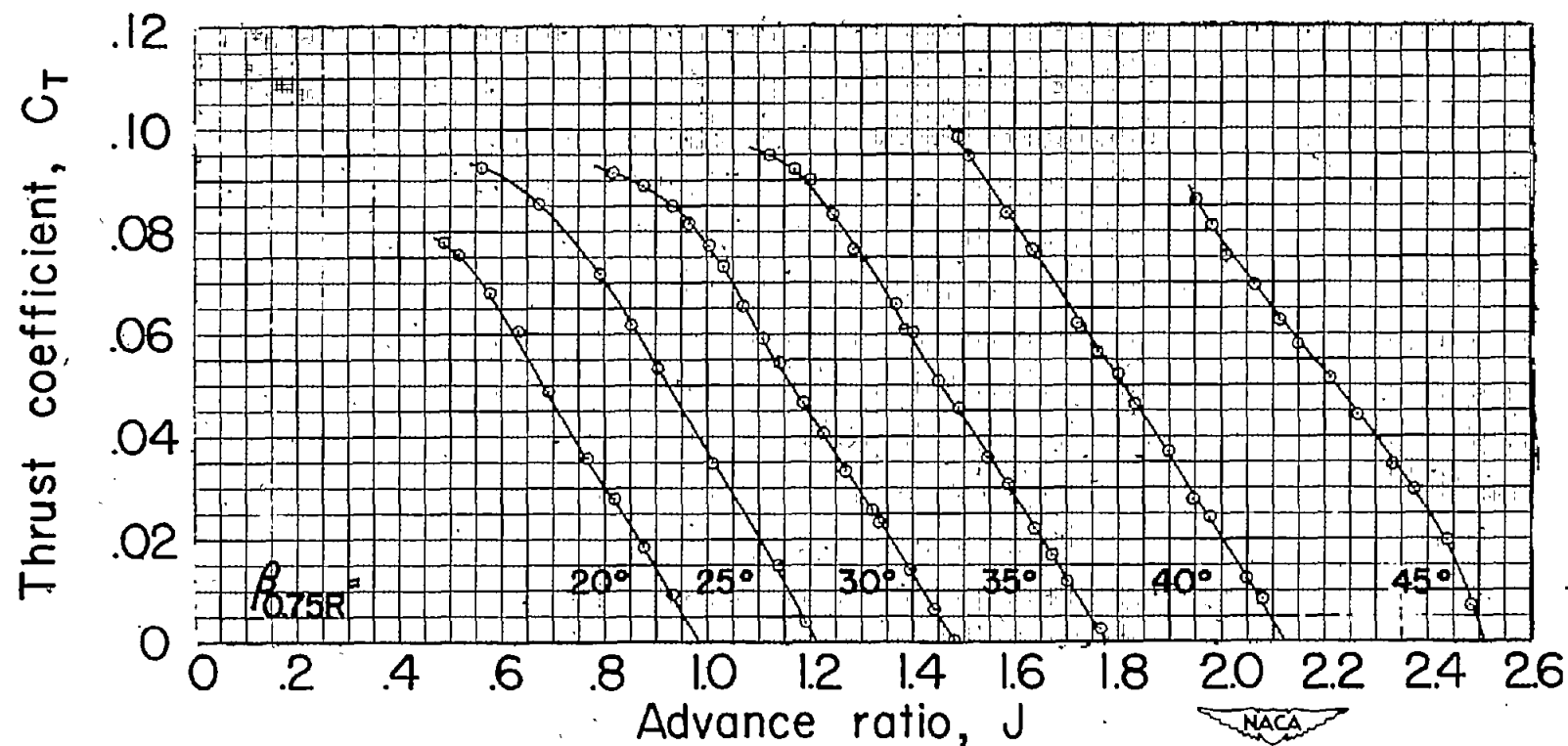


Figure 21.- Characteristics of NACA 10-(3)(08)-03 propeller. Rotational speed, 1,500 rpm; $\beta_0.75R = 45^\circ$.



(a) Thrust coefficient.

Figure 22.- Characteristics of NACA 10-(3)(08)-03 propeller. Rotational speed, 1,600 rpm.

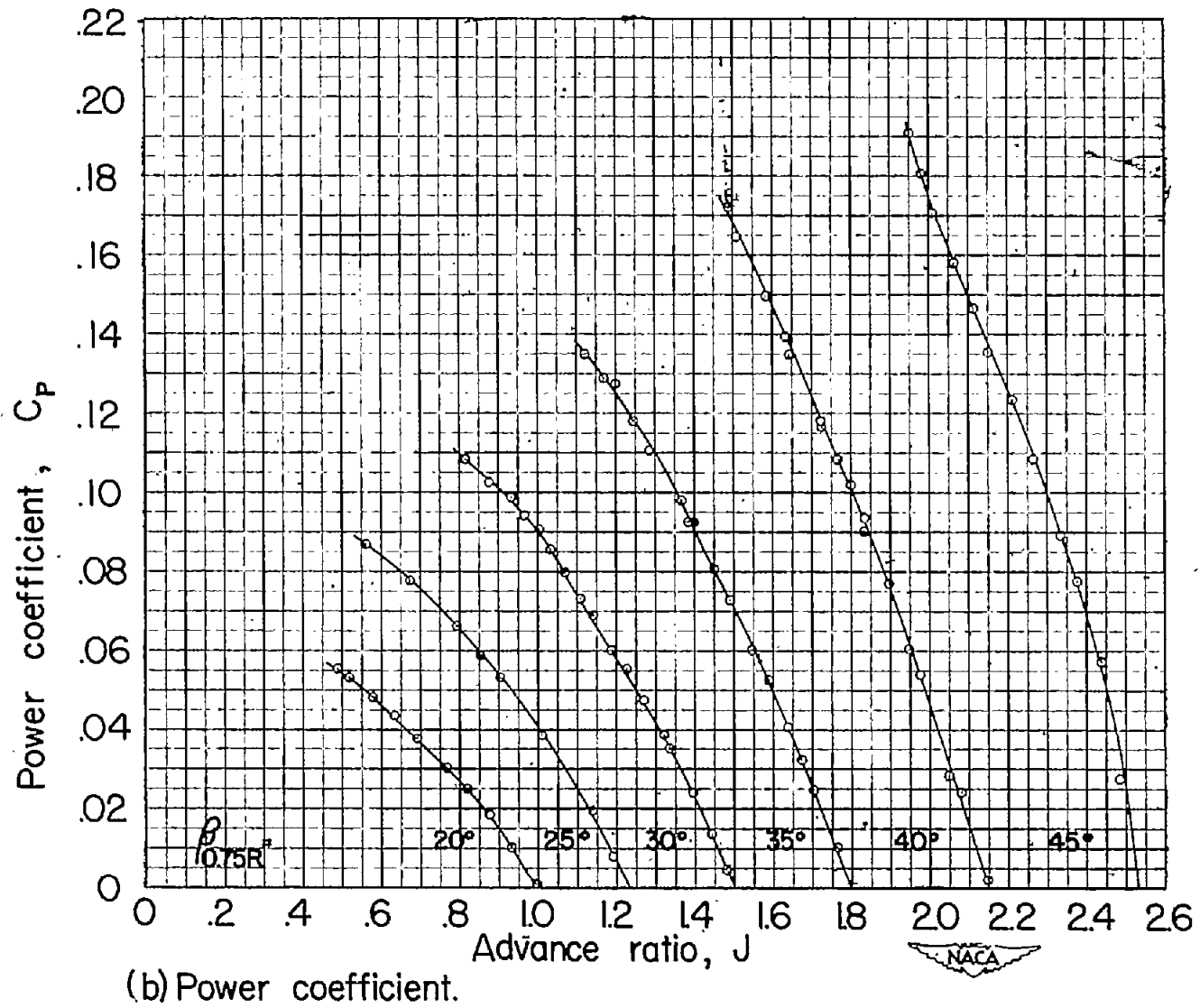
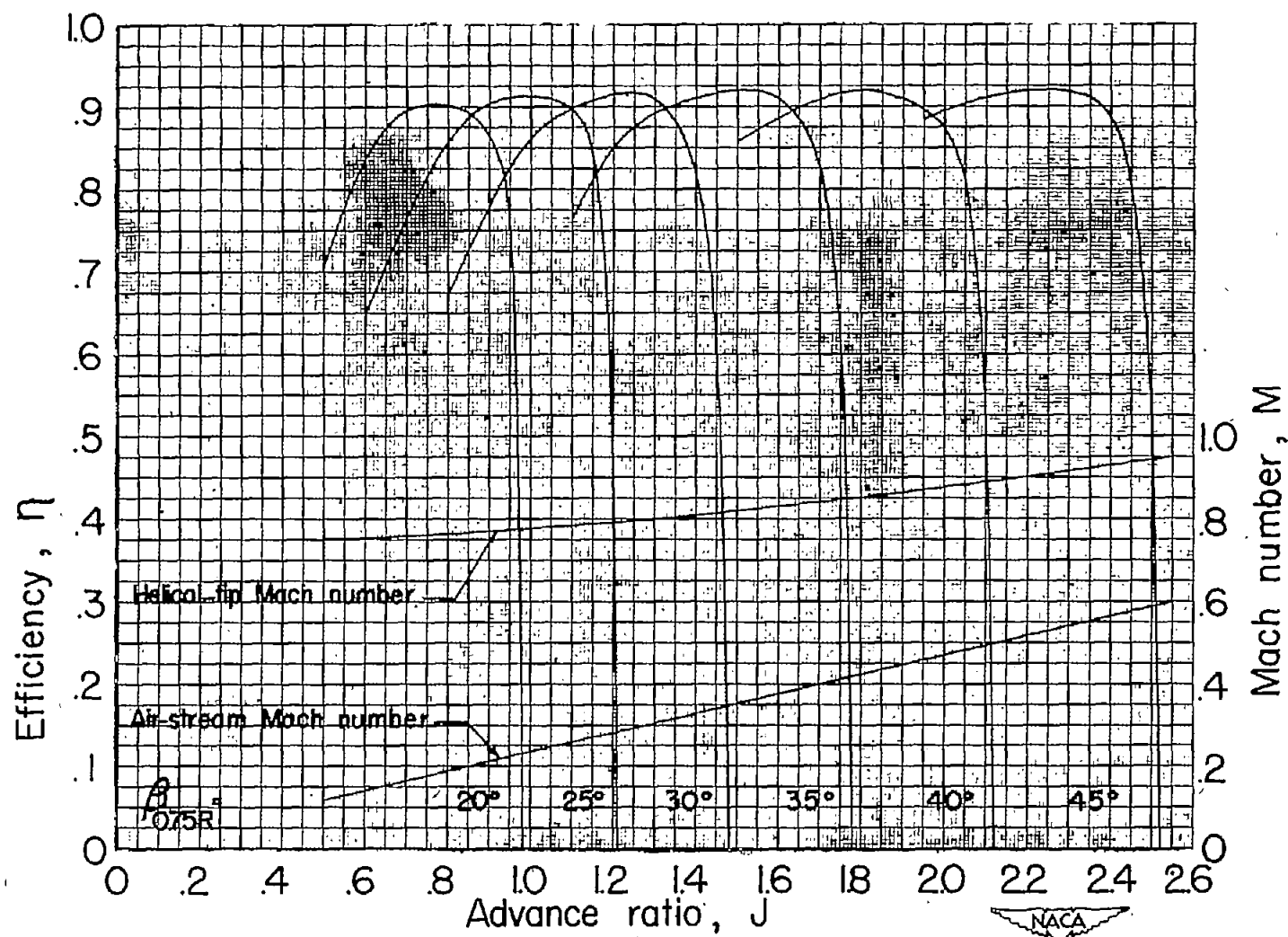
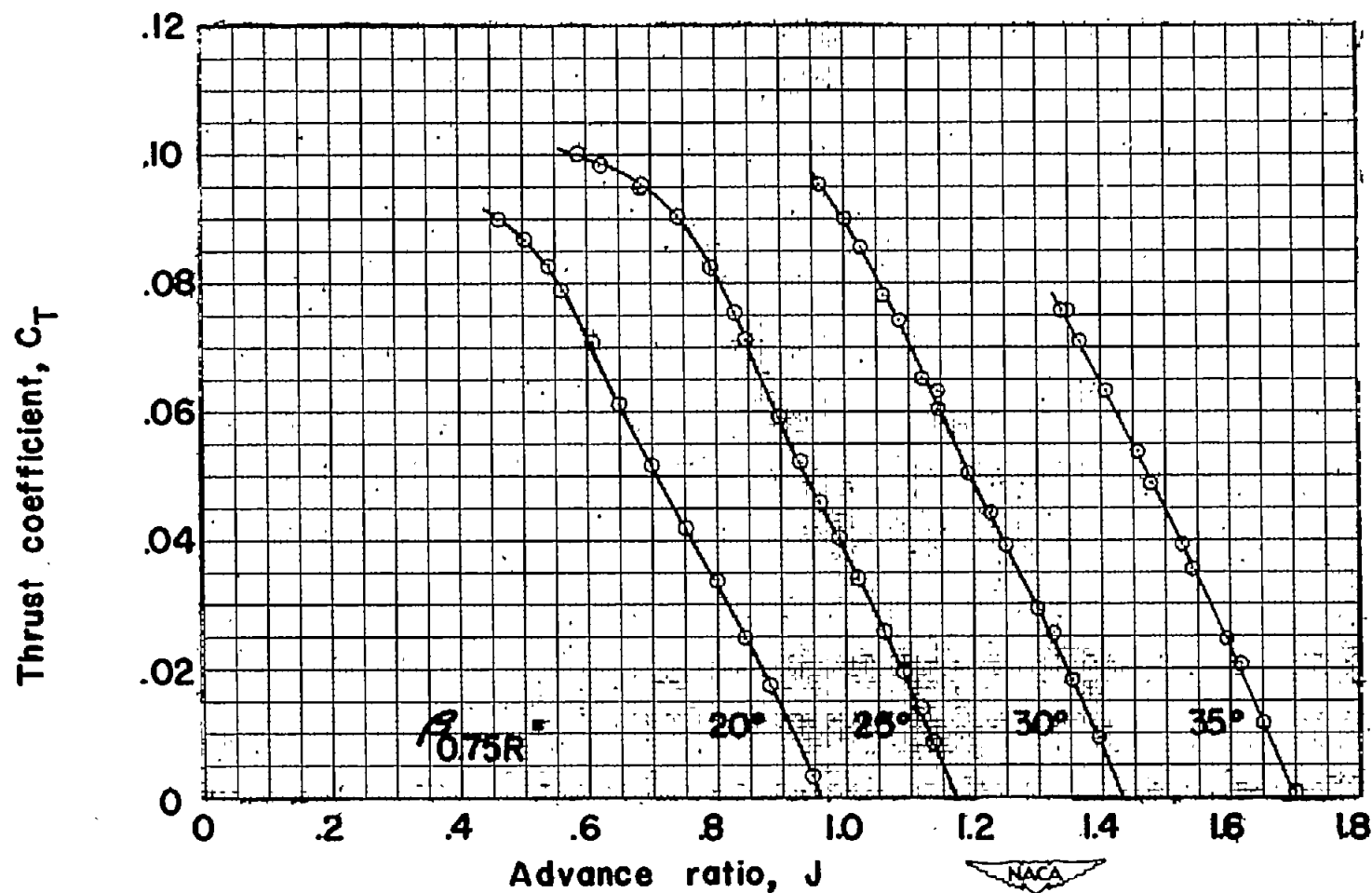


Figure 22.- Continued. Rotational speed, 1,600 rpm.



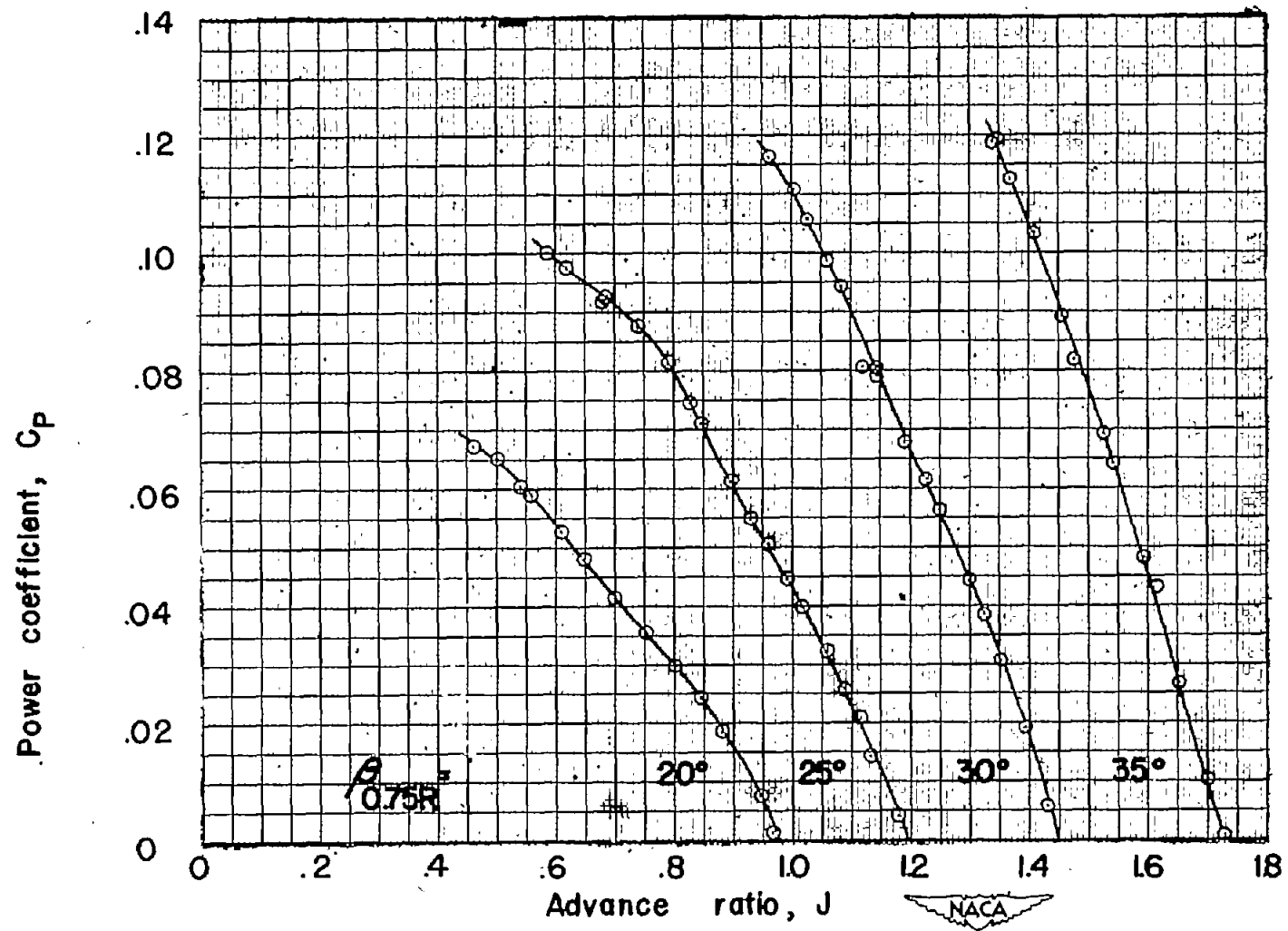
(c) Efficiency.

Figure 22.- Concluded. Rotational speed, 1,600 rpm.



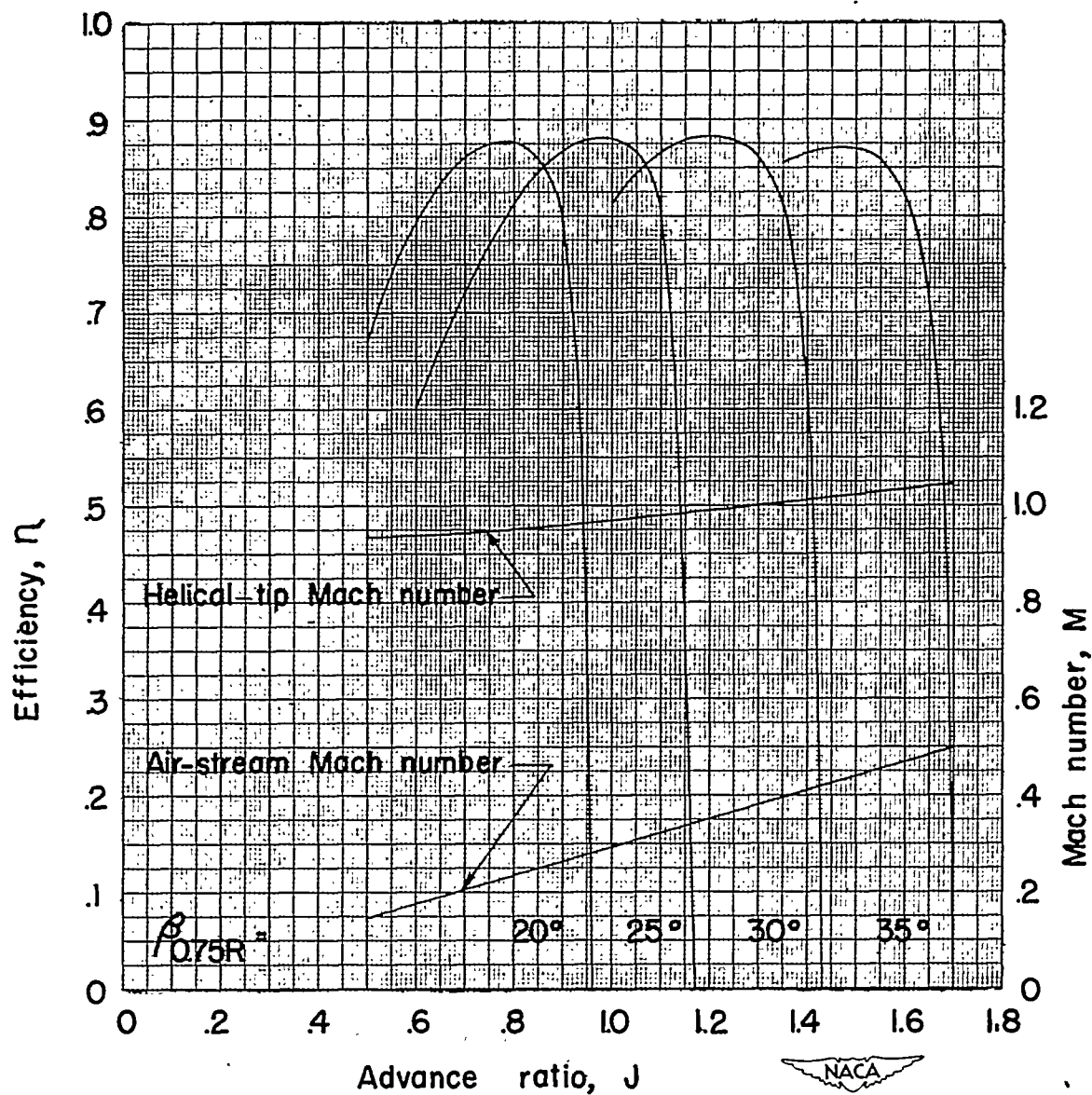
(a) Thrust coefficient.

Figure 23.- Characteristics of NACA 10-(3)(08)-03 propeller. Rotational speed, 2,000 rpm.



(b) Power coefficient.

Figure 23.- Continued. Rotational speed, 2,000 rpm.



(c) Efficiency.

Figure 23.- Concluded. Rotational speed, 2,000 rpm.

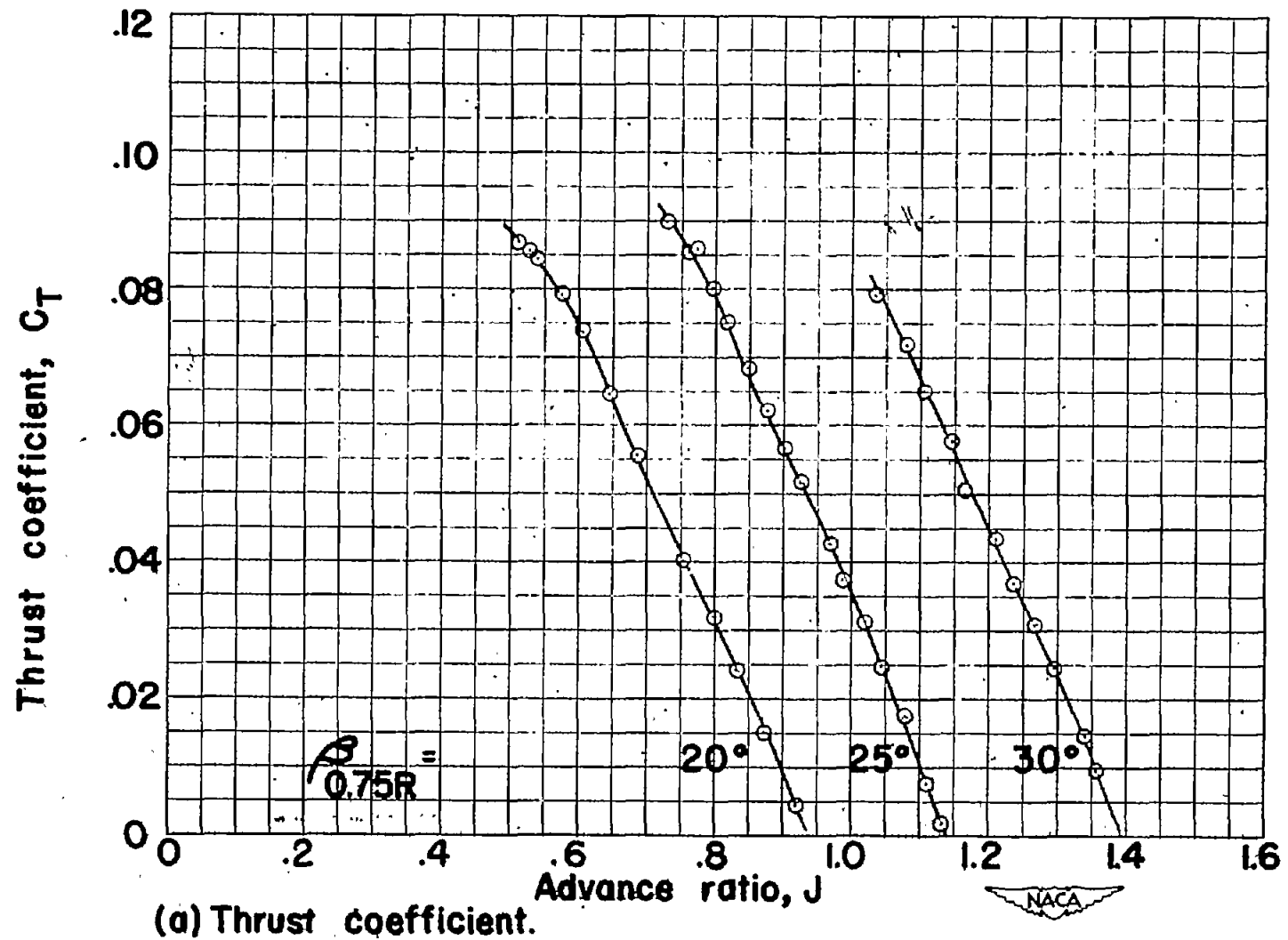
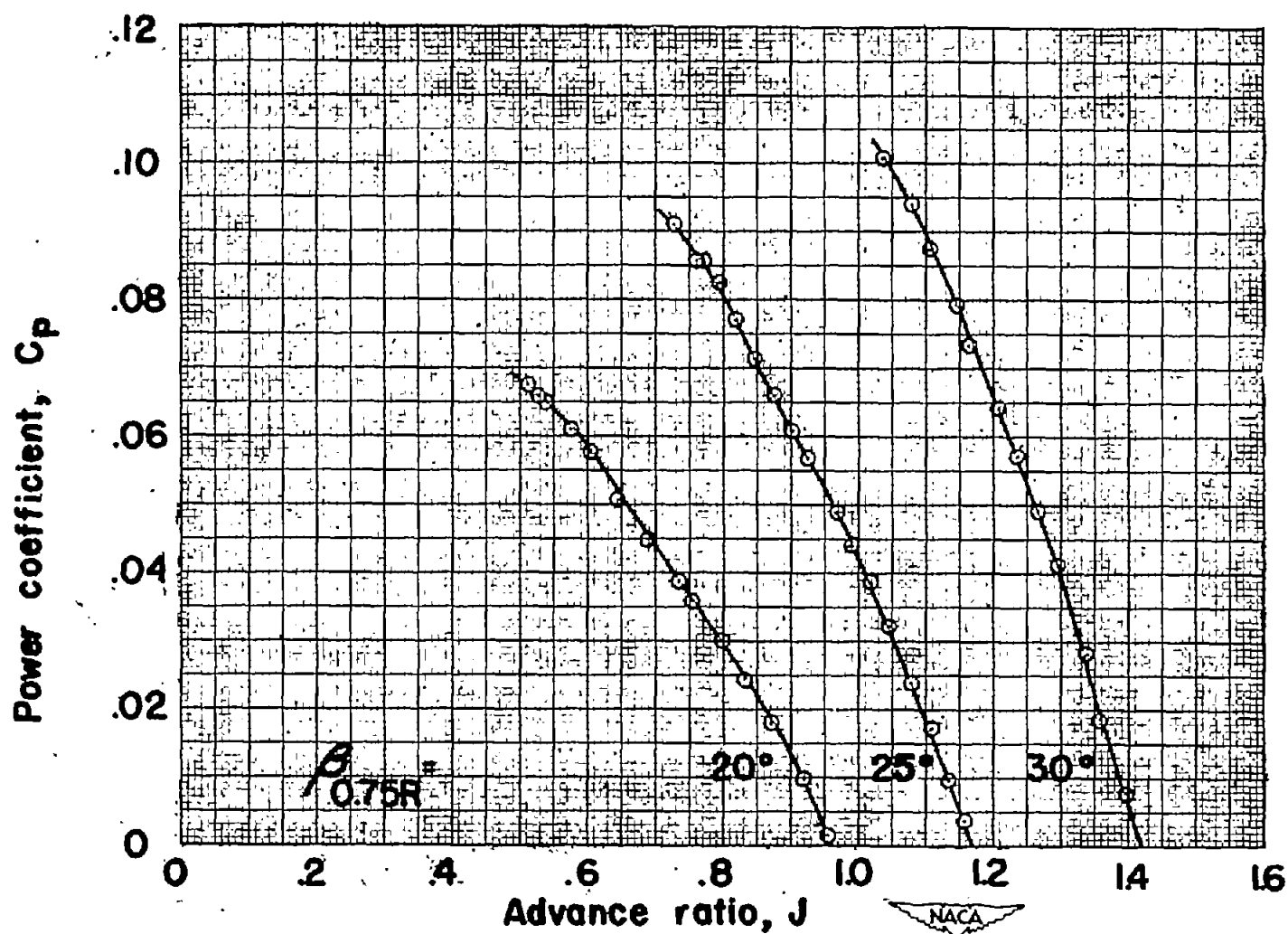
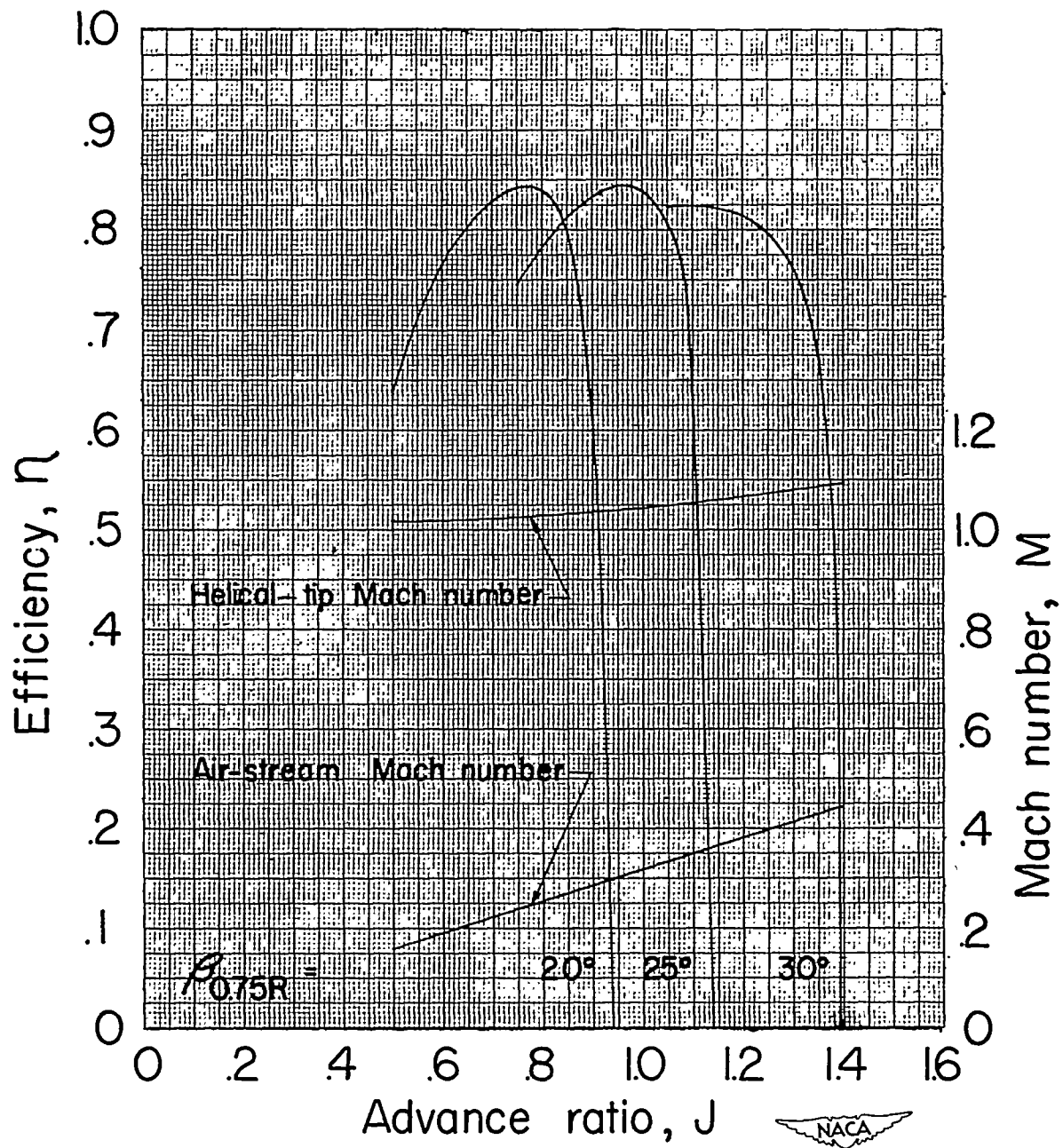


Figure 24.- Characteristics of NACA 10-(3)(08)-03 propeller. Rotational speed, 2,160 rpm.



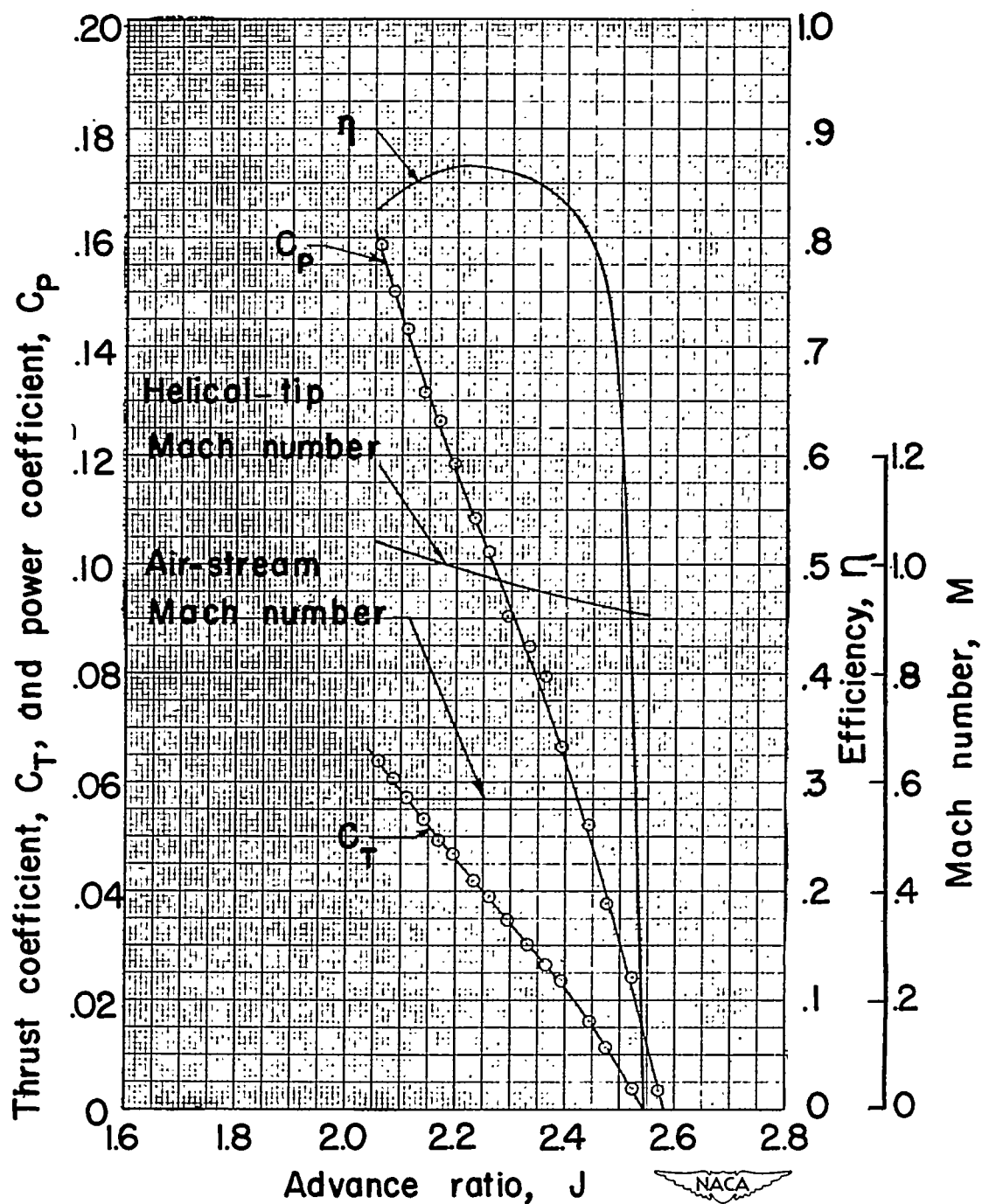
(b) Power coefficient.

Figure 24.- Continued. Rotational speed, 2,160 rpm.



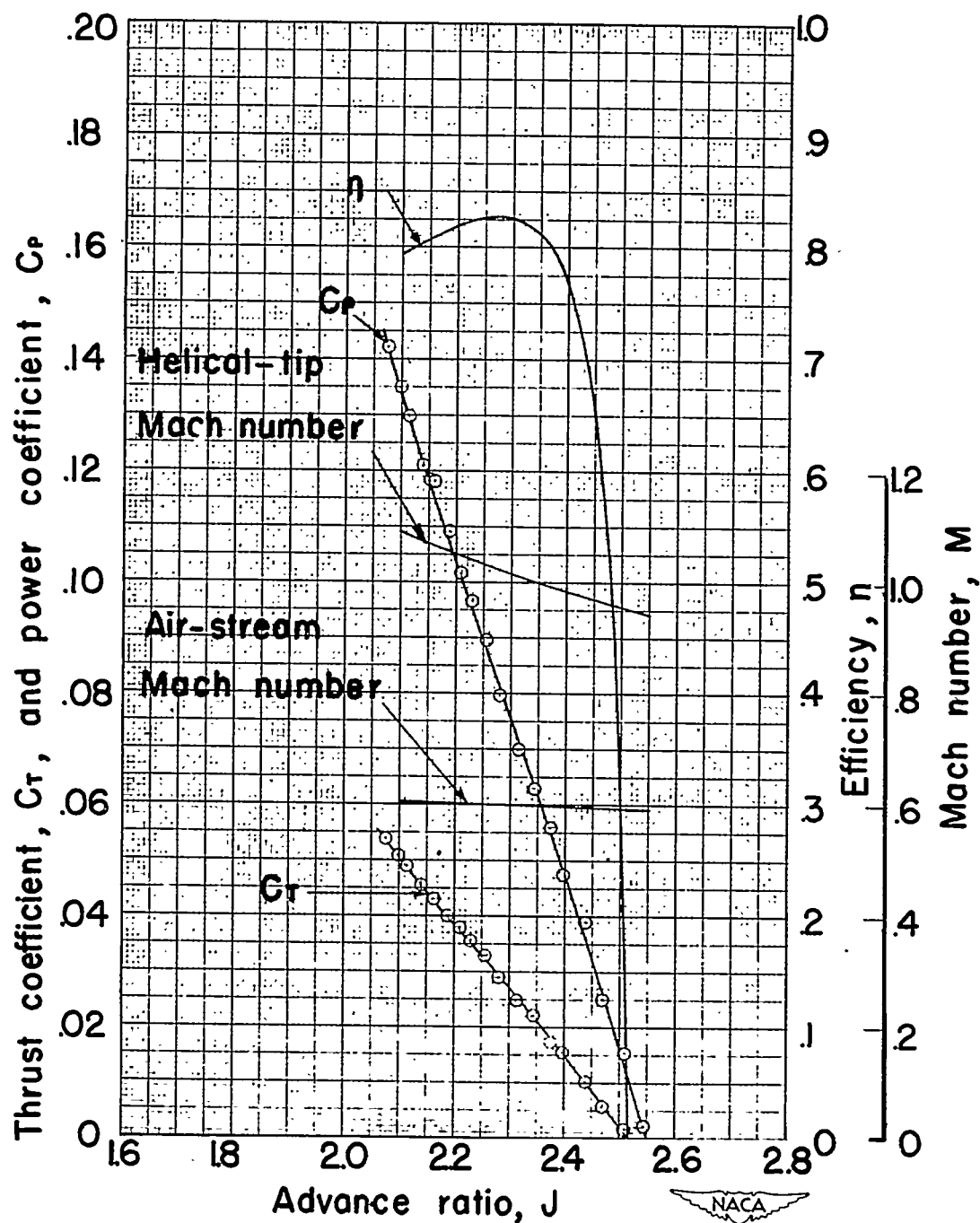
(c) Efficiency.

Figure 24.- Concluded. Rotational speed, 2,160 rpm.



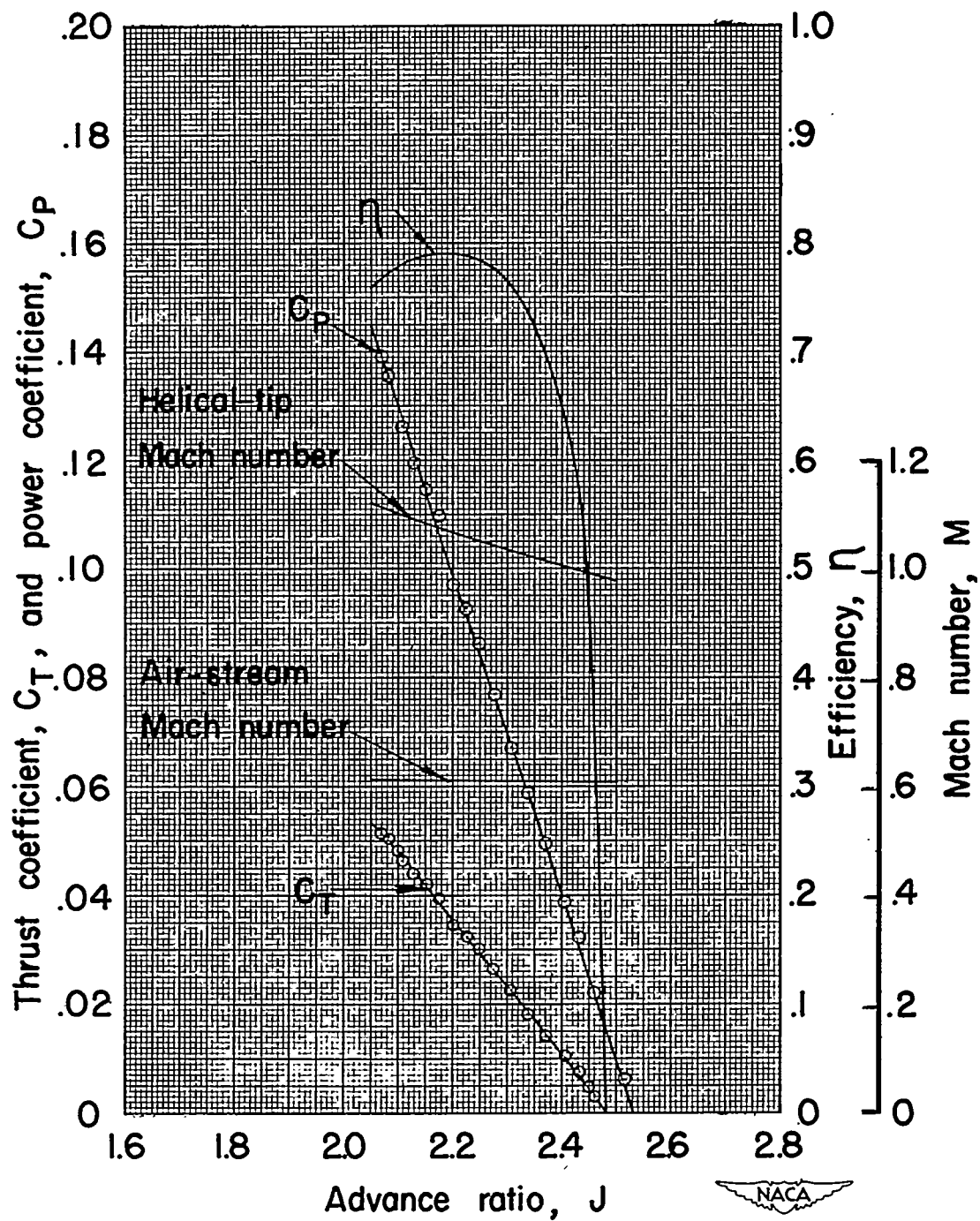
(a) Air-stream Mach number at maximum efficiency, 0.57.

Figure 25.- Characteristics of NACA 10-(3)(08)-03 propeller at high forward speeds. $\beta_{0.75R} = 45^\circ$.



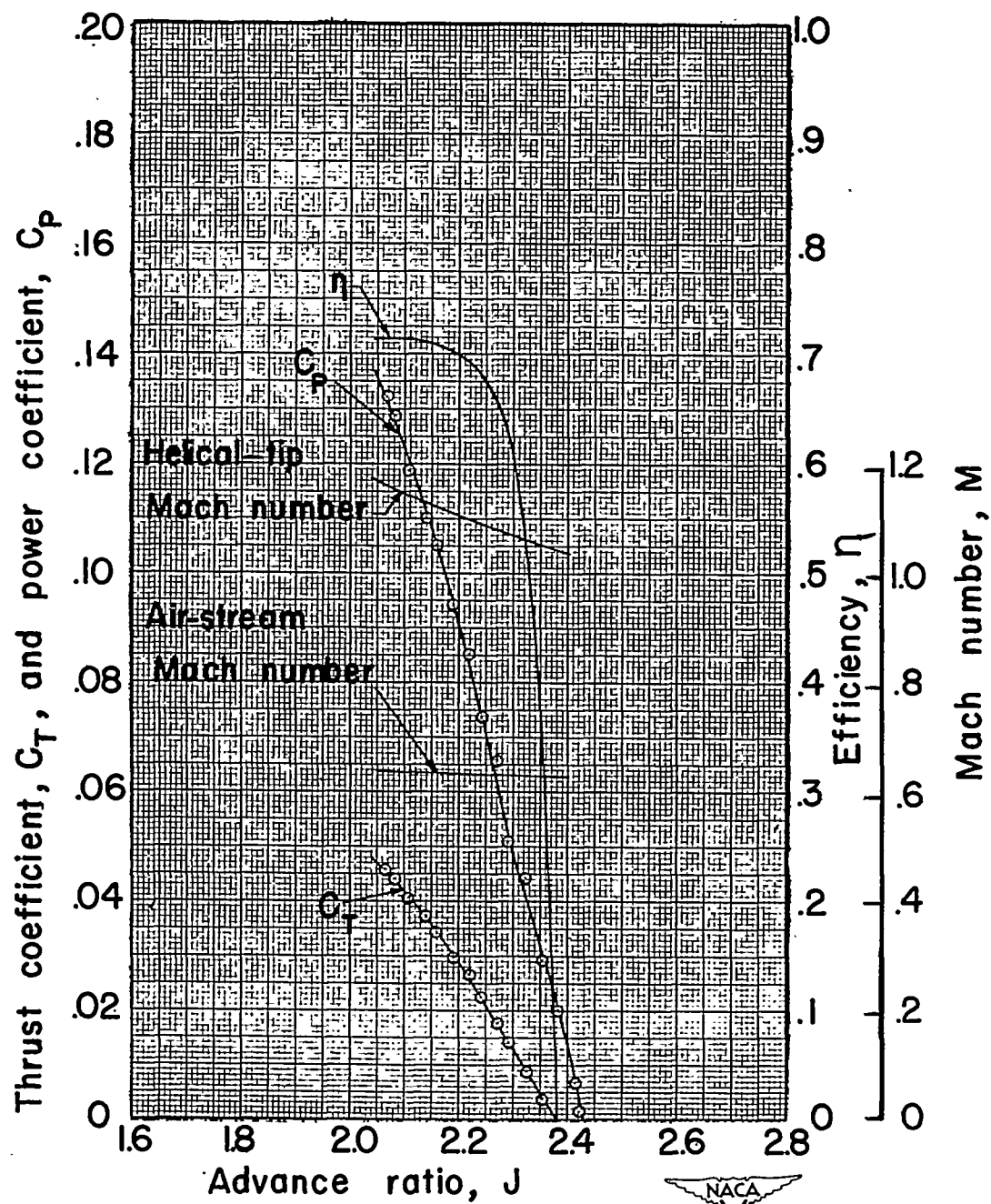
(b) Air-stream Mach number at maximum efficiency, 0.601.

Figure 25.- Continued.



(c) Air-stream Mach number at maximum efficiency, 0.612.

Figure 25.- Continued.



(d) Air-stream Mach number at maximum efficiency, 0.638.

Figure 25.- Concluded.

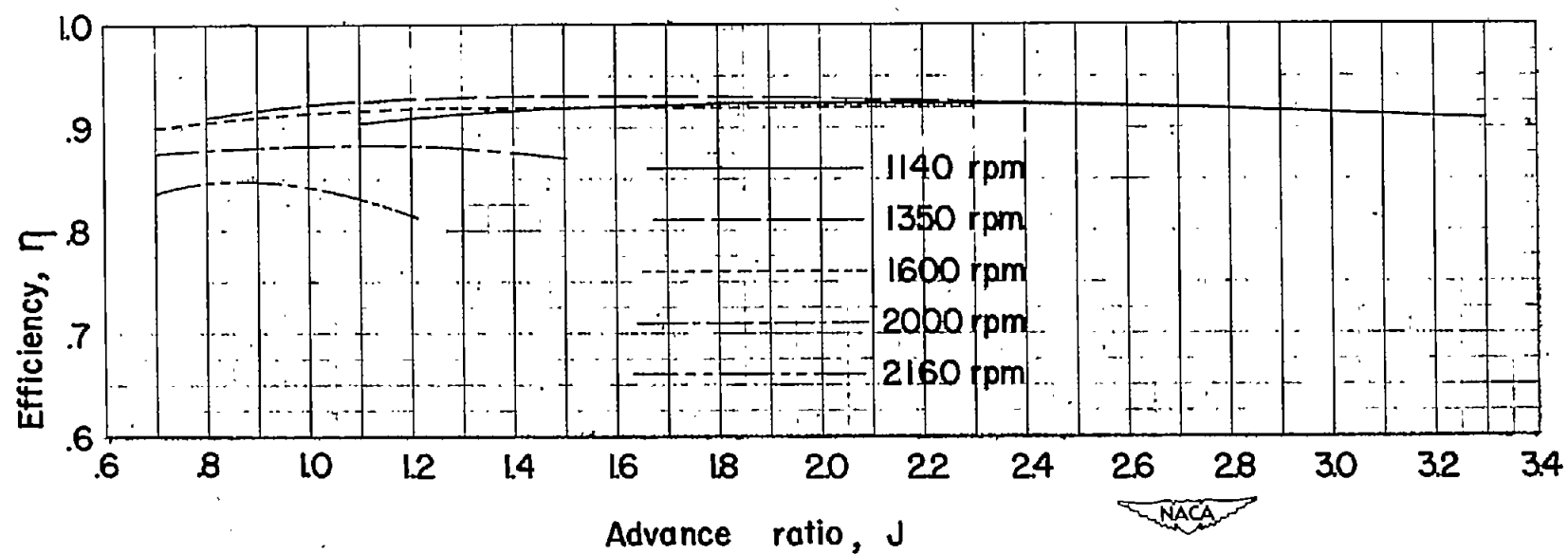


Figure 26.- Envelope efficiency of NACA 10-(3)(08)-03 propeller.

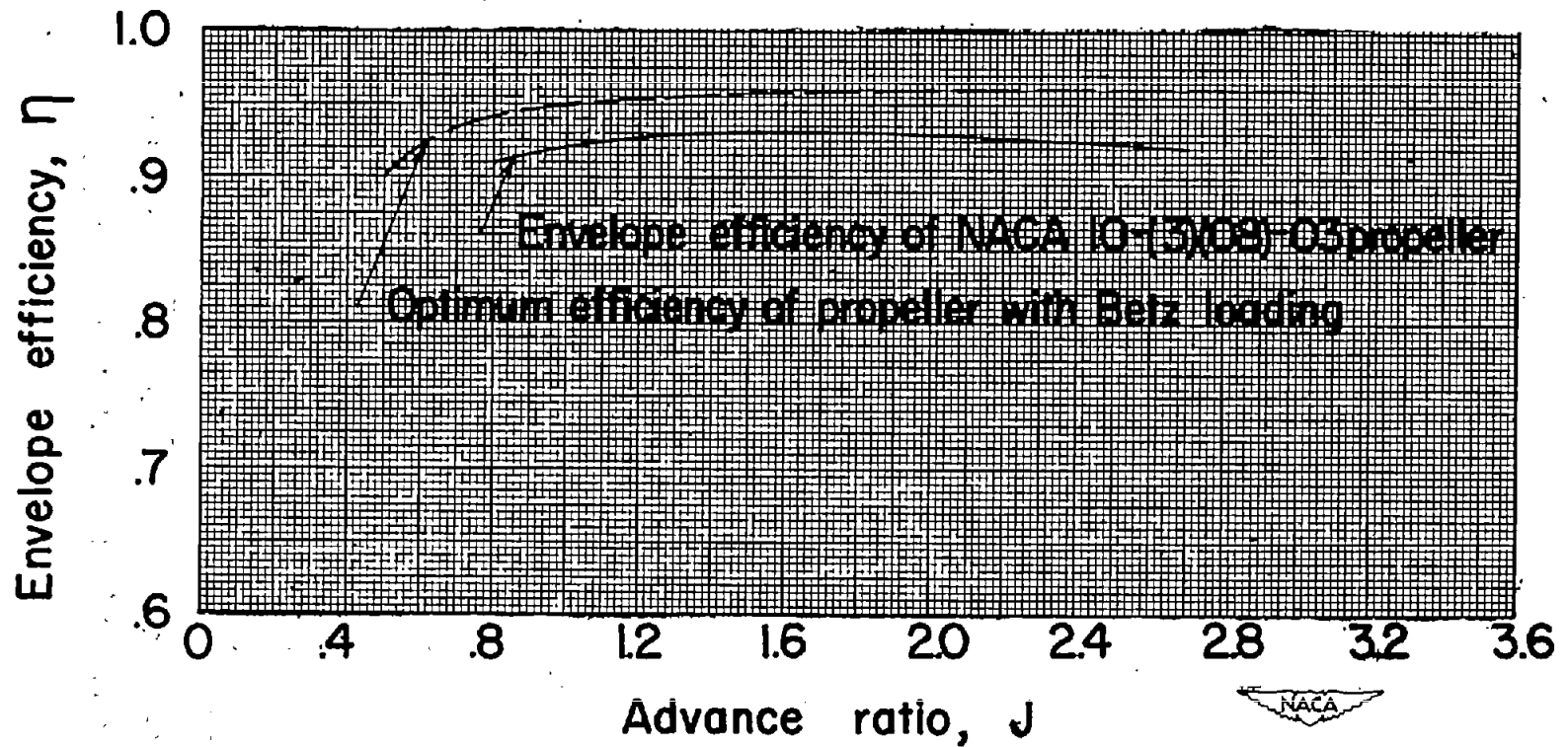


Figure 27.- Comparison of the envelope efficiency of NACA 10-(3)(08)-03 propeller at 1,350 rpm with the optimum efficiency of a two-blade propeller with the Betz loading.

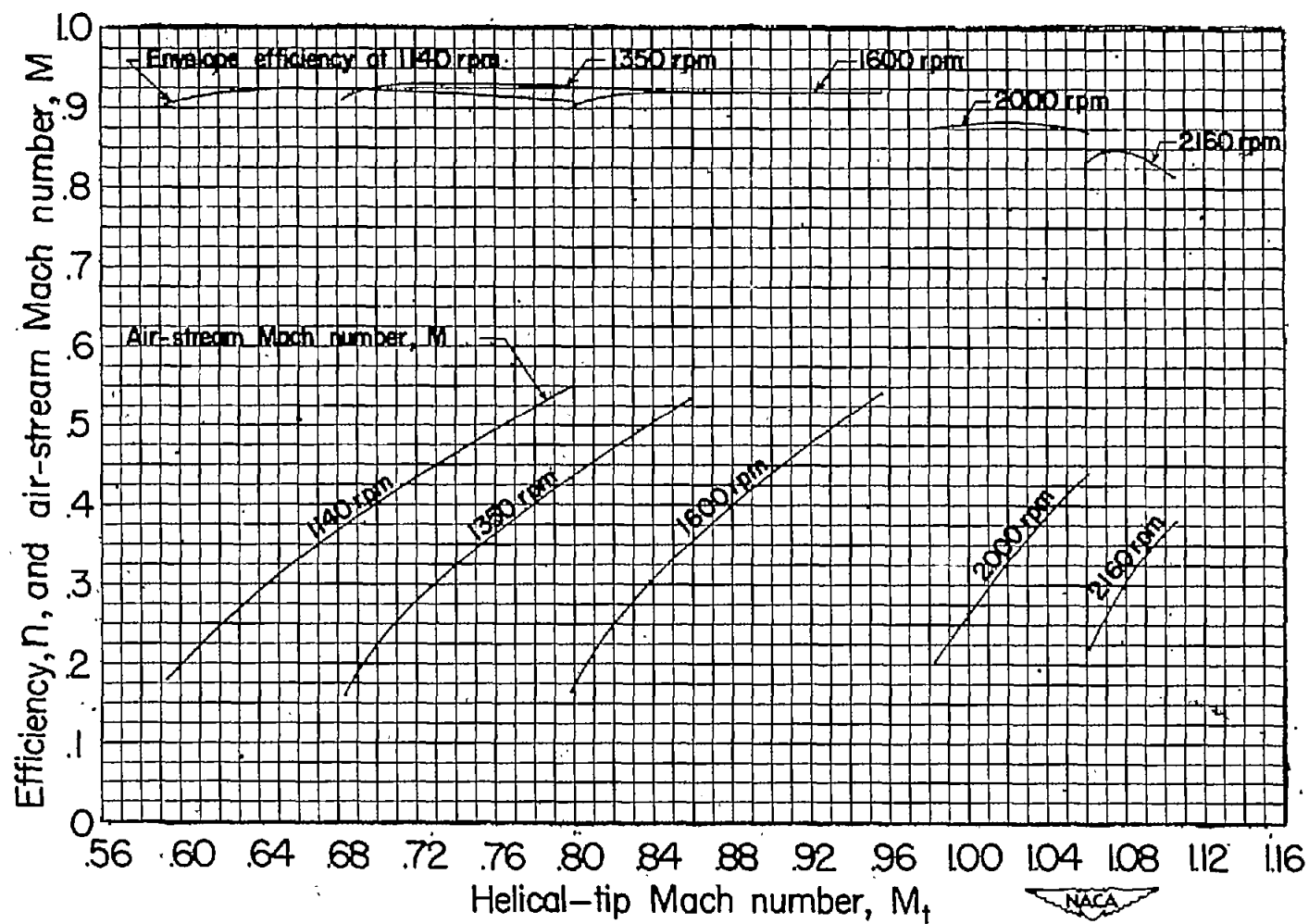


Figure 28.- Effect of compressibility on envelope efficiency for NACA 10-(3)(08)-03 propeller.

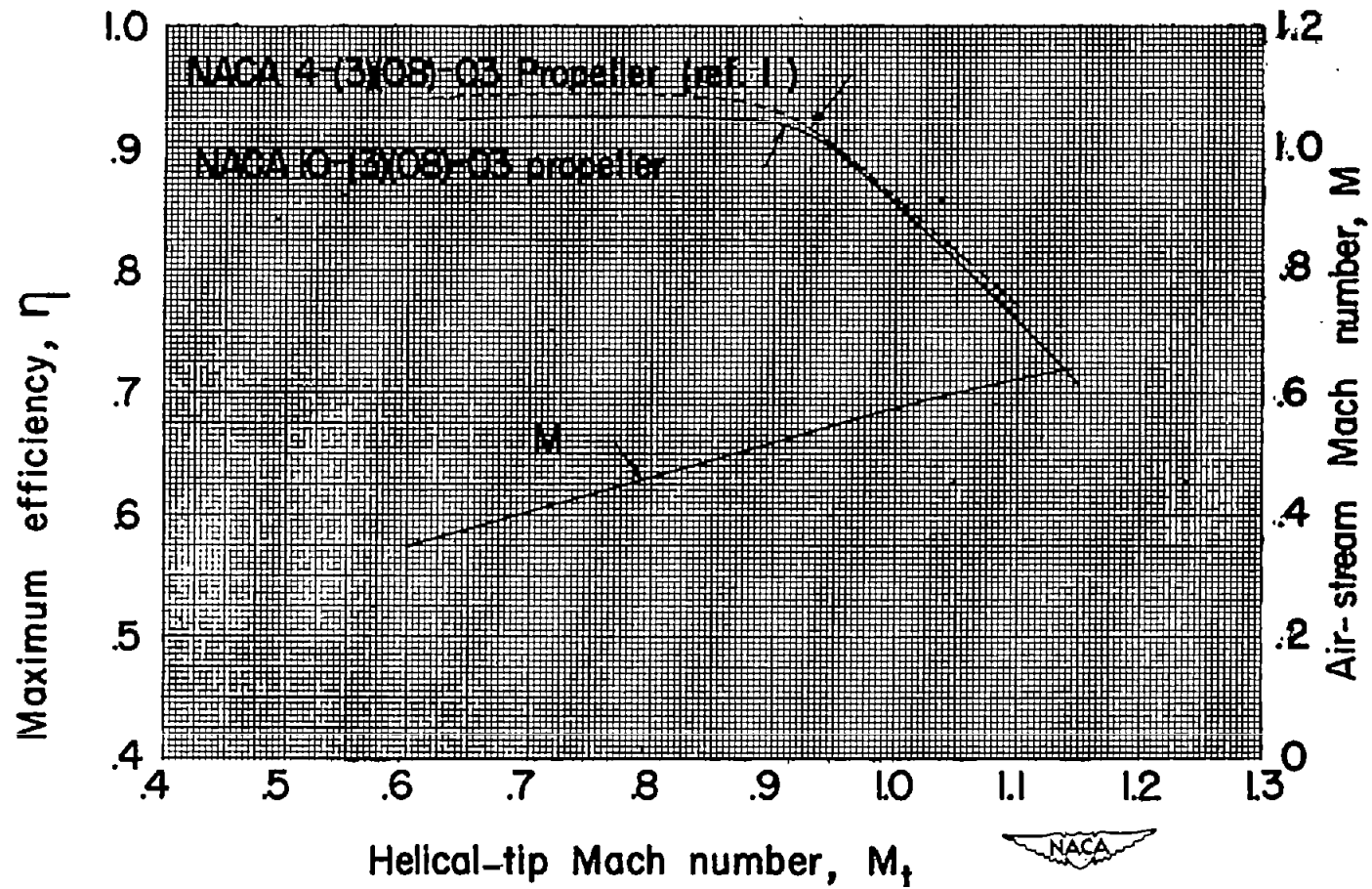


Figure 29.- Effect of compressibility on maximum efficiency. $\beta_{0.75R} = 45^\circ$.

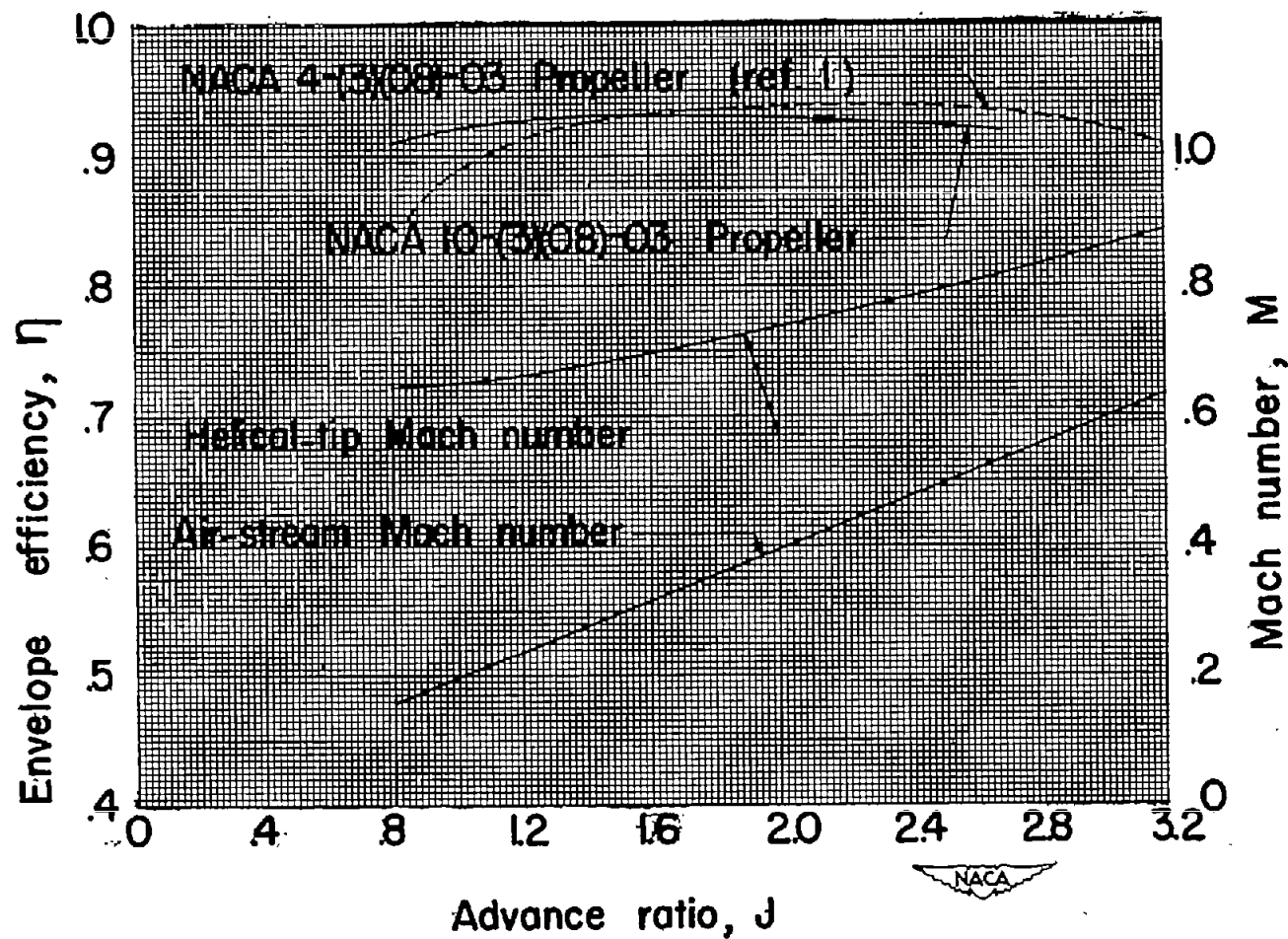


Figure 30.- Comparison of envelope efficiency for NACA 10-(3)(08)-03 and 4-(3)(08)-03 propellers.

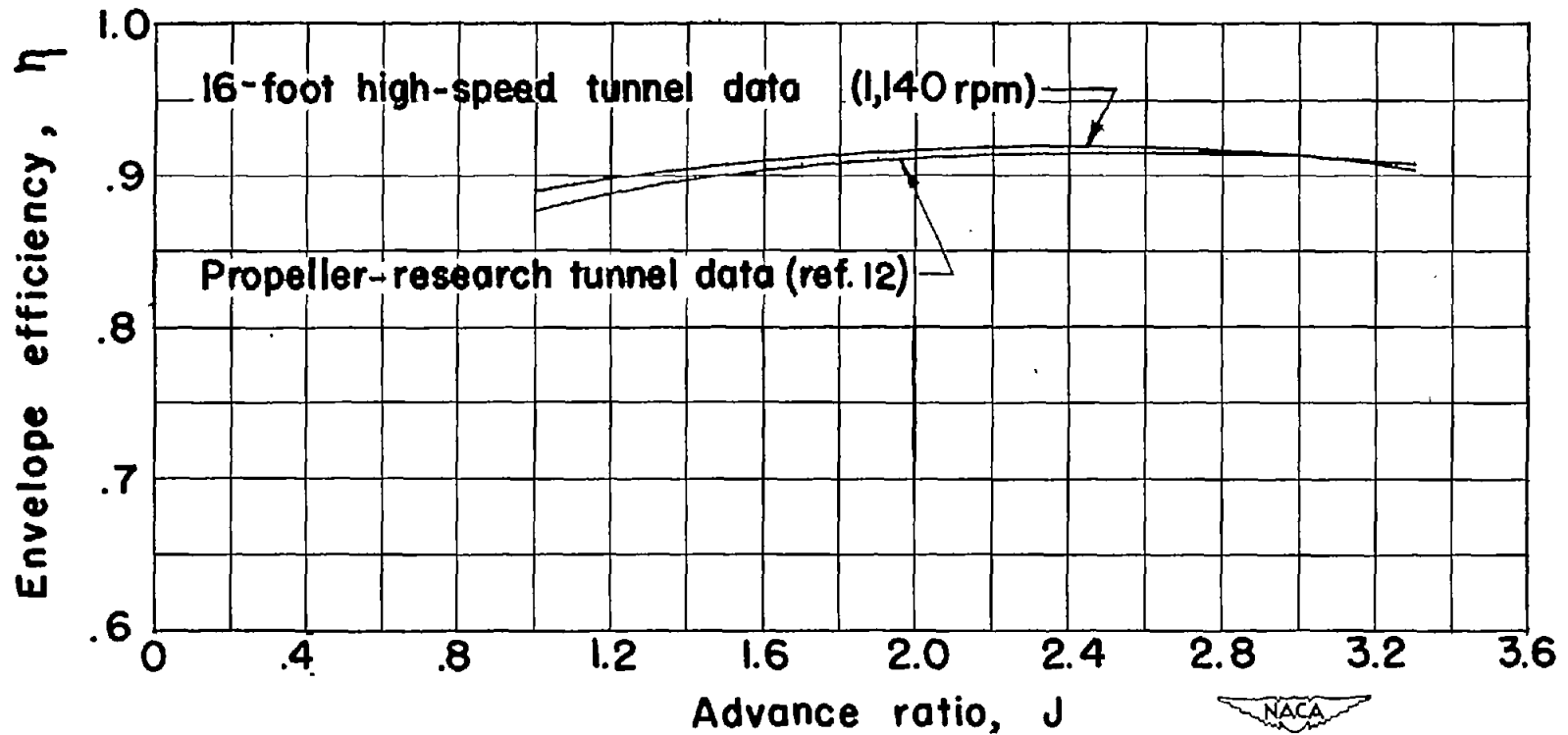
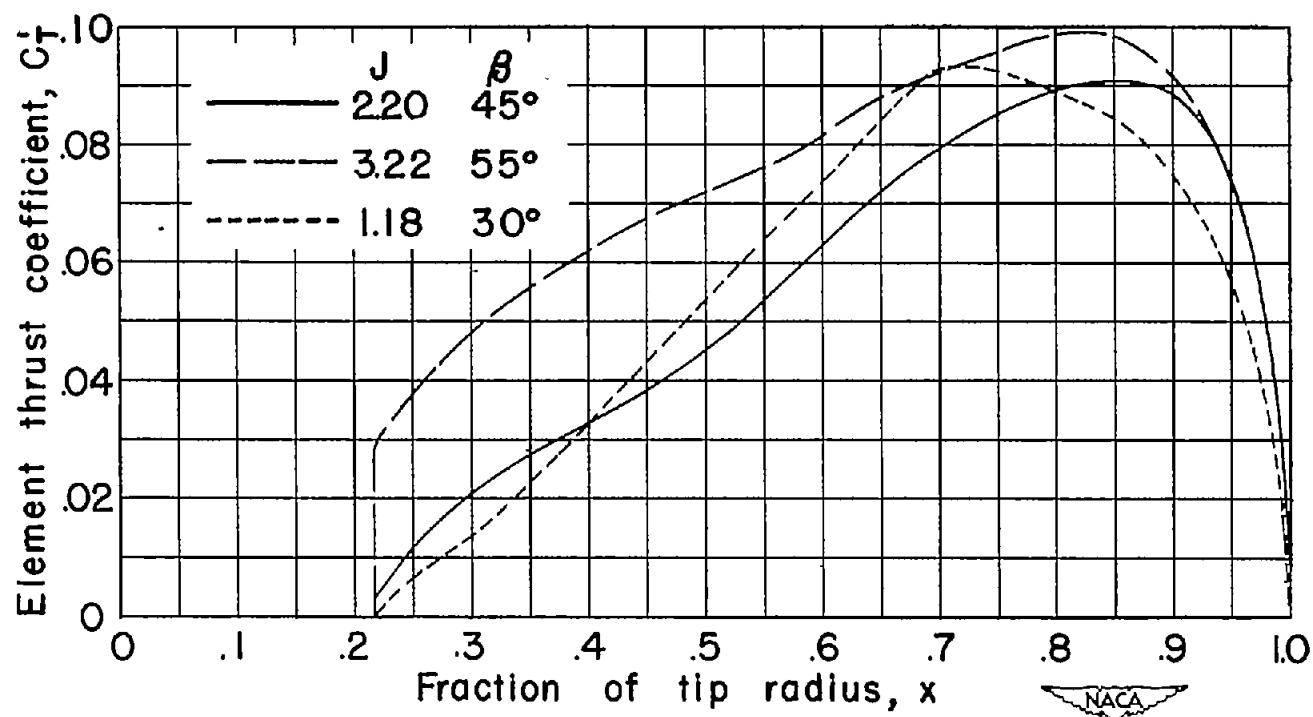
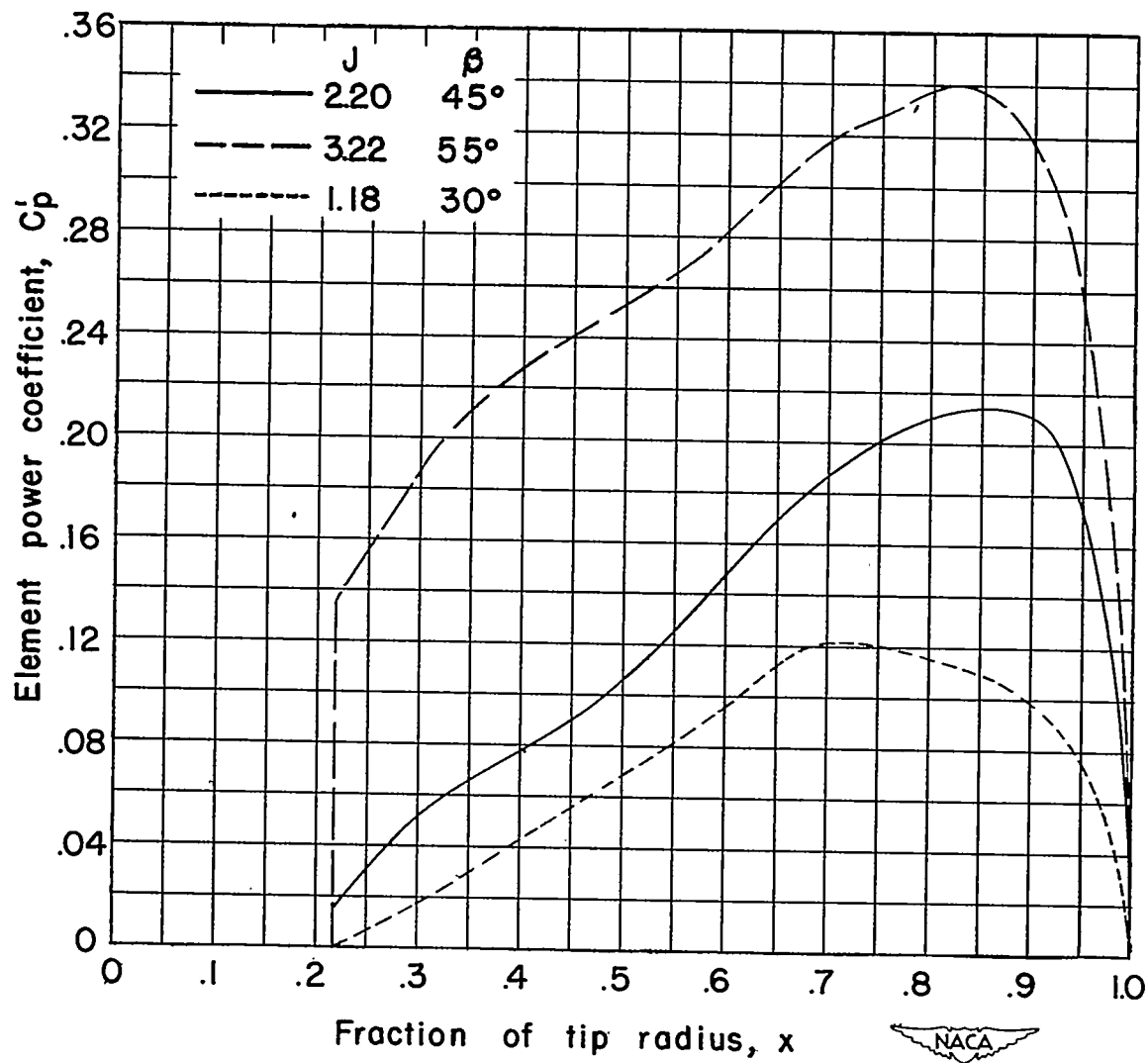


Figure 31.- Comparison of the envelope efficiency obtained in the Langley propeller-research tunnel and in the Langley 16-foot high-speed tunnel for a three-blade NACA 10-(3)(08)-03 propeller.



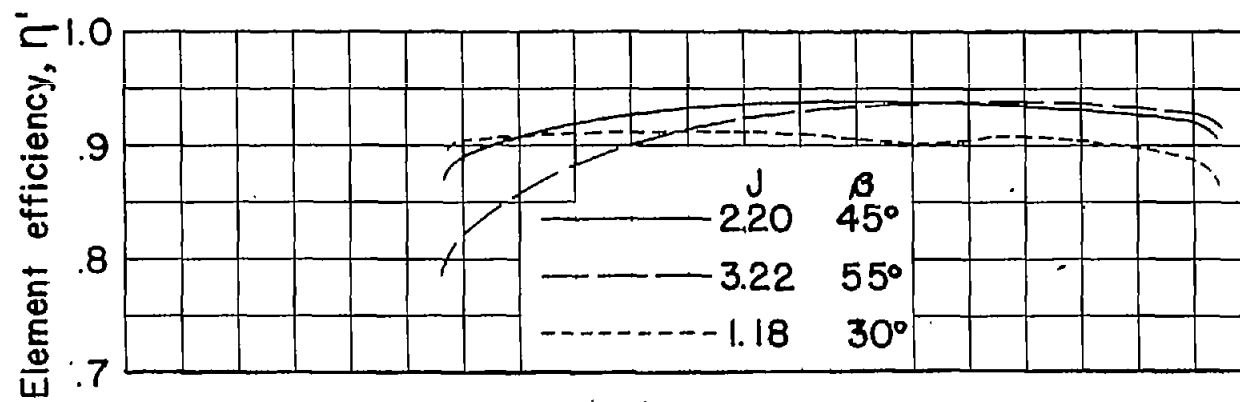
(a) Thrust coefficient.

Figure 32.- Calculated distribution of thrust coefficient, power coefficient, efficiency, and Mach number along the NACA 10-(3)(08)-03 propeller blade at 1,140 rpm.

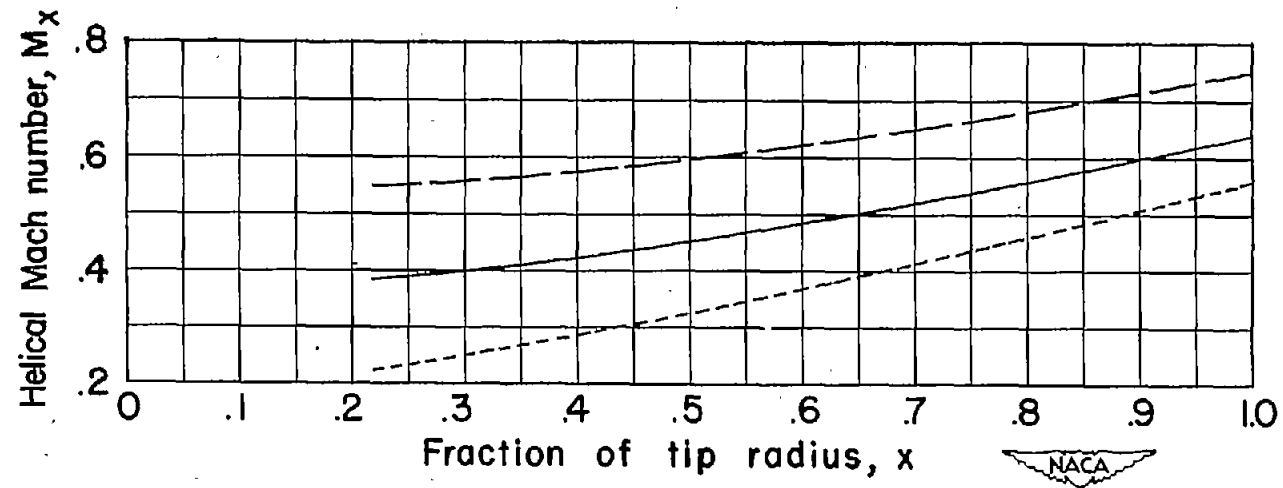


(b) Power coefficient.

Figure 32.- Continued.



(c) Efficiency.



(d) Mach number.

Figure 32.- Concluded.

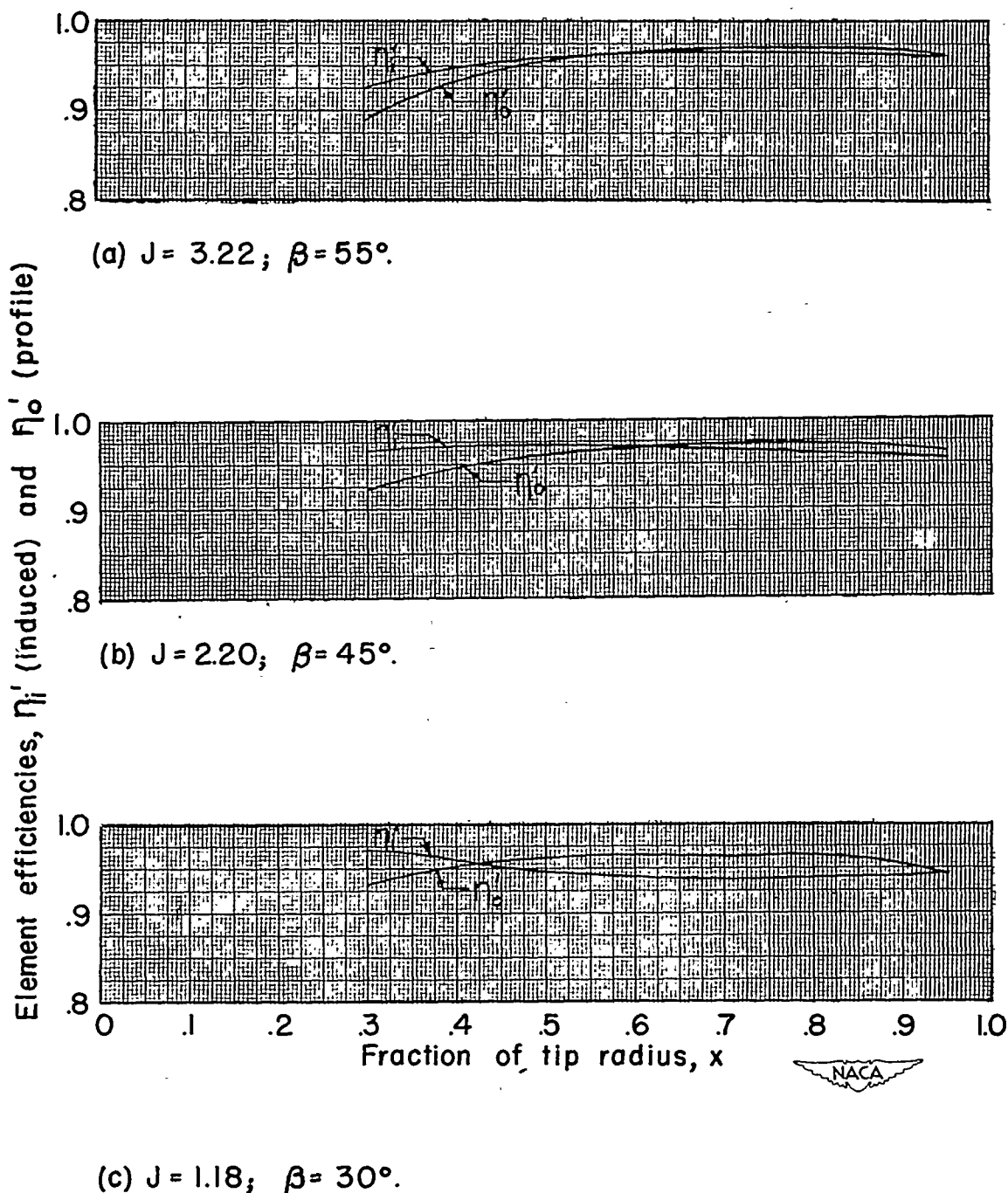


Figure 33.- Calculated distribution of induced and profile efficiencies along the NACA 10-(3)(08)-03 propeller blade at 1,140 rpm.

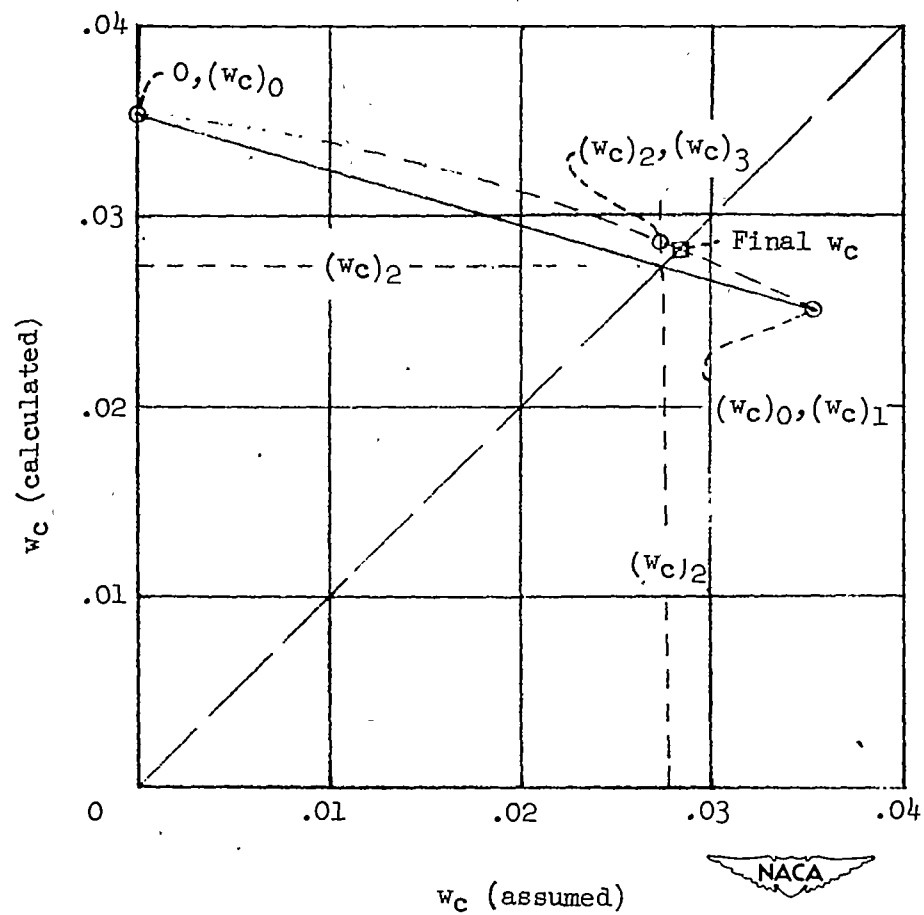


Figure 35.- Graph used in the solution for w_c by successive approximations.